

THE LARGE-SCALE SDSS LRG 3-POINT CORRELATION FUNCTION

FELIPE MARÍN^{1,2}

Draft version November 5, 2018

ABSTRACT

We present new measurements of the redshift-space three-point correlation function (3PCF) of Luminous Red Galaxies (LRGs) from the Sloan Digital Sky Survey (SDSS). Using the largest dataset to date, the Data Release 7 (DR7) LRGs, and an improved binning scheme compared to previous measurements, we measure the LRG 3PCF on large scales up to $\sim 90 h^{-1}\text{Mpc}$, from the mildly non-linear to quasi-linear regimes. Comparing the LRG correlations to the dark matter two- and three-point correlation functions, obtained from N-body simulations we infer linear and non-linear bias parameters. As expected, LRGs are highly biased tracers of large scale structure, with a linear bias $b_1 \sim 2$; the LRGs also have a large positive non-linear bias parameter, in agreement with predictions of galaxy population models. The use of the 3PCF to estimate biasing helps to also make estimates of the cosmological parameter σ_8 , as well as to infer best-fit parameters of the Halo Occupation Distribution parameters for LRGs. We also use a large suite of public mock catalogs to characterize the error covariance matrix for the 3PCF and compare the variance among simulation results with jackknife error estimates.

Subject headings: cosmology: large-scale structure of the universe, observations, high-order clustering

1. INTRODUCTION

The large-scale structure traced by galaxies is shaped both by cosmic expansion history, which determines the gravitational evolution of density perturbations, and by the physics of galaxy formation. Comparison of galaxy clustering with the predictions of structure formation models therefore constrains both cosmological and galaxy formation parameters. For a given clustering observable, e.g., the galaxy two-point correlation function (2PCF), $\xi_{gg}(r)$, there are typically significant degeneracies between the inferred cosmological and galaxy formation parameters. Measurement of multiple observables with different relative dependencies on cosmology and galaxy formation can help break such degeneracies (Abazajian et al. 2005; Zheng & Weinberg 2007). The galaxy three-point correlation function (3PCF), the next level up in the hierarchy of N -point correlation functions, encodes information that is complementary to that contained in the 2PCF and is therefore a useful second observable for constraining cosmology and galaxy formation (Sefusatti & Scoccimarro 2005; Sefusatti et al. 2006).

The 3PCF has been measured since the advent of the first angular catalogs (Peebles & Groth 1975), and more recently in the last generation of spectroscopic surveys such as 2dFGRS (Jing & Börner 2004; Gaztañaga et al. 2005), and SDSS (Kayo et al. 2004; Nichol et al. 2006; Kulkarni et al. 2007; McBride et al. 2010). The goals of these efforts have been mostly to test predictions from theories of growth of structure and cosmological simulations, as well as to measure the biasing of the galaxies with respect to the dark matter 3PCF. With the large

volume of current surveys, we are able to improve the signal-to-noise of the measurements, and obtain more information from the 3PCF to help constrain cosmological and galaxy formation models.

In this paper, we measure the 3PCF for a particular class of galaxies, the Luminous Red Galaxies (LRGs) (Eisenstein et al. 2001) observed spectroscopically by the Sloan Digital Sky Survey (SDSS) (York et al. 2000), and use the results to constrain galaxy bias and cosmological parameters. LRGs offer several advantages for this measurement. At the bright end of the galaxy luminosity function, LRGs can be targeted out to relatively large distances, $z \sim 0.5$ (whereas the average redshift is $z \sim 0.3$), in the SDSS spectroscopic survey. Their clustering can therefore be measured over scales large compared to those probed by L_* galaxies in the same survey (Eisenstein et al. 2005; Tegmark et al. 2006; Percival et al. 2007; Gaztañaga et al. 2009b), which are on average at $z \sim 0.1$. In addition, LRGs are more strongly clustered than less-luminous galaxies, making their correlations intrinsically easier to measure on large scales, where shot-noise is subdominant.

The physics of galaxy formation is imprinted in the N -point galaxy correlation functions via the bias, the relation between the spatial distributions of galaxies and dark matter. Although the Halo Occupation Distribution model (HOD, see for instance Jing et al. 1998; Seljak 2000; Scoccimarro et al. 2001; Berlind & Weinberg 2002; Cooray & Sheth 2002; Zheng et al. 2005) has become a popular framework for parametrizing the bias (especially on small scales), here we focus on using the 2PCF and 3PCF LRG measurements on large scales to constrain a simpler, non-linear, local bias model that appears to adequately capture the features displayed by the clustering data. This approach allows us to break the degeneracy that exists between the linear bias parameter and the r.m.s of density fluctuations at scale of $8 h^{-1}\text{Mpc}$, σ_8 , when extracting information from the 2PCF, as shown,

¹ Department of Astronomy & Astrophysics and Kavli Institute for Cosmological Physics, The University of Chicago, Chicago, IL 60637 USA

² Centre for Astrophysics & Supercomputing, Swinburne University of Technology, PO Box 218, Hawthorn, VIC 3122, Australia; fmarin@astro.swin.edu.au

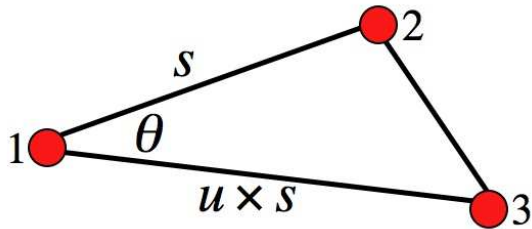


FIG. 1.— Parametrization of triangles for measuring the three-point correlation function.

using different statistics, in Pan & Szapudi (2005) and Ross et al. (2008). Although a complete and detailed HOD analysis using fits to the 2-point and 3-point functions will be presented elsewhere (Sabiú et al. 2010), we explore the idea of using the LRG bias parameters in constraining HOD models, as suggested by Sefusatti & Scoccimarro (2005).

We note that Gaztañaga et al. (2009a) have recently measured the SDSS LRG 3PCF on very large scales, focusing on detection of the baryon acoustic oscillation signature. Reid & Spergel (2009) used a counts-in-cylinders statistic to constrain the LRG HOD. In addition, Ross et al. (2008) measured higher-order angular clustering of a sample of photometrically selected LRGs from the SDSS and used it to constrain non-linear bias parameters and get constraints on σ_8 .

Our goal here is to present an up-to-date measurement of the 3PCF, show another way to use the 3PCF information on large scales, in this case to calculate the bias, and offer complementary constraints on σ_8 , and show that we can use the 3PCF as a complement to find best-fit HOD parameters.

The outline of the paper is as follows. In §2 we review the 3PCF and describe our binning scheme for the 3PCF measurement; we also describe the SDSS LRG sample and the simulations used to create mock catalogs. In §3 we present our measurements of the 3PCF in the LRG sample. In §4 we discuss the estimation of 3PCF errors, which are critical in constraining parameters. In §5 we constrain the non-linear bias parameters of the LRGs and explore the possibility of constraining the matter power spectrum amplitude σ_8 , as well as relevant HOD parameters. We summarize and conclude in §6.

2. METHODS, DATA & SIMULATIONS

2.1. The 3-point correlation function

The 3PCF describes the probability of finding three objects in a particular triangle configuration, compared to that of a random sample. The joint probability of finding three objects in three infinitesimal volumes dV_1 , dV_2 , and dV_3 is given by (Peebles 1980)

$$P = [1 + \xi(r_{12}) + \xi(r_{23}) + \xi(r_{31}) + \zeta(r_{12}, r_{23}, r_{31})] \times \bar{n}^3 dV_1 dV_2 dV_3, \quad (1)$$

where \bar{n} is the mean density of objects, ξ is the 2PCF, and ζ is the (connected) 3PCF:

$$\xi(r_{12}) = \langle \delta(r_1) \delta(r_2) \rangle \quad (2)$$

$$\zeta(r_{12}, r_{23}, r_{31}) = \langle \delta(r_1) \delta(r_2) \delta(r_3) \rangle; \quad (3)$$

where δ is the fractional overdensity of objects or the continuous field studied. The triangle sides r_{ij}

are the distances between objects i and j in the triplet. Since the 3PCF depends upon the configuration of the three sides, it is sensitive to the shapes of spatial structures (Sefusatti & Scoccimarro 2005; Gaztañaga & Scoccimarro 2005; Marín et al. 2008). Since the ratio ζ/ξ^2 is both predicted and found to be close to unity over a large range of length scales even though ξ and ζ each vary by orders of magnitude (Peebles 1980), it is convenient to define the reduced 3PCF,

$$Q(s, u, \theta) \equiv \frac{\zeta(s, u, \theta)}{\xi(r_{12})\xi(r_{23}) + \xi(r_{23})\xi(r_{31}) + \xi(r_{31})\xi(r_{12})}. \quad (4)$$

Here, $s \equiv r_{12}$ sets the scale size of the triangle, and the shape parameters are given by the ratio of two sides of the triangle, $u \equiv r_{23}/r_{12}$, and the angle between those two sides, $\theta = \cos^{-1}(\hat{r}_{12} \cdot \hat{r}_{23})$, where \hat{r}_{12} , \hat{r}_{23} are unit vectors in the directions of those sides (see Figure 1). By measuring the shape- and scale-dependence of $Q(s, u, \theta)$ for galaxies and comparing with that predicted for dark matter, we can constrain the galaxy bias.

We calculate the 2PCF using the estimator of Landy & Szalay (1993),

$$\xi = \frac{DD - 2DR + RR}{RR}. \quad (5)$$

Here, DD is the number of data pairs normalized by $N_D \times N_D/2$, DR is the number of pairs using data and random catalogs normalized by $N_D N_R$, and RR is the number of random data pairs normalized by $N_R \times N_R/2$, where N_D and N_R are the number of points in the data and in the random catalog, respectively. The 3PCF is calculated using the Szapudi & Szalay (1998) estimator:

$$\zeta = \frac{DDD - 3DDR + 3DRR - RRR}{RRR}, \quad (6)$$

where DDD , the number of data triplets, is normalized by $N_D^3/6$, and RRR , the random data triplets, is normalized by $N_R^3/6$. DDR is normalized by $N_D^2 N_R/2$, and DRR by $N_D N_R^2$. These estimators optimally correct for edge effects by incorporating pair and triplet counts from a random catalog. To compute the correlation functions, we use the *NPT* software developed in collaboration with the Auton Lab at Carnegie Mellon University. *NPT* is a fast implementation of N -point correlation function estimation using multi-resolution kd-trees to compute the number of pairs and triplets in a dataset. For more details and information on the algorithm, see Moore et al. (2001), Gray et al. (2004), and Nichol et al. (2006).

2.2. Measuring the 3PCF: Binning

Since measurements of two- and three-point correlations involve counts of pairs and triplets of objects, the question arises of how to choose the bins of pair and triplet separation (Gaztañaga & Scoccimarro 2005; Nichol et al. 2006; Kulkarni et al. 2007; Marín et al. 2008). Small bins enable measurements with fine resolution in separation and the possible identification of features in the correlation functions but at the cost of large shot noise due to the small numbers of pairs and triplets per bin. Large bins reduce the shot noise but tend to wash out features of the 3PCF. The optimal bin

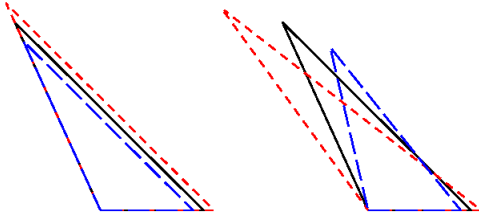


FIG. 2.— Comparison of two binning schemes for the 3PCF measurement. *Left*: bins in r_{ij} used in this paper, with $\Delta r_{ij} = 0.1r_{ij}$; *Right*: bins in s, u, θ , with $\Delta s = 0.1s$, $\Delta u = 0.1$, $\Delta\theta = \pi/100$. Black (solid) triangles show the central configuration for the bin, with $u = 2$ and $\theta = 100^\circ$. Blue (long dashed) triangles are the smallest triangles in that bin. Red (short dashed) triangles are the largest in the bin. For the r_{ij} bins, the largest and smallest triangles in the bin are similar to the central triangle.

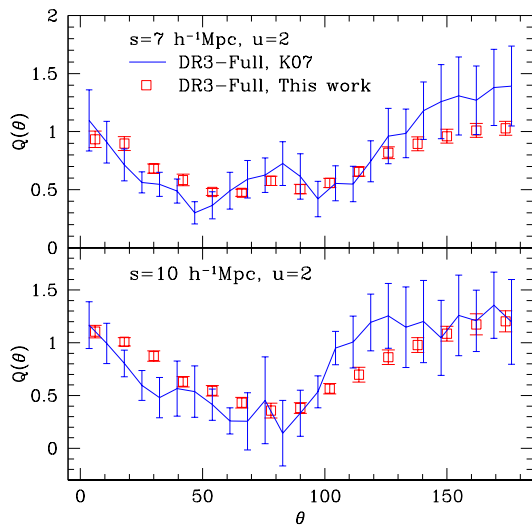


FIG. 3.— Comparison of two binning schemes for the DR3 LRG 3PCF measurement. DR3 Sample LRG reduced 3PCF in for $s = 7 h^{-1}\text{Mpc}$ (top) and $s = 10 h^{-1}\text{Mpc}$ (bottom) with similar resolution but different binning schemes. Blue solid line represents 3PCF from the scheme used in (Kulkarni et al. 2007, K07 in the plot) and open squares used the binning representation used in this paper. Diagonal errors obtained from jack-knife resampling method.

size is therefore a compromise and depends on the relative importance of signal-to-noise vs. resolution for the question at hand.

For the 3PCF, there is also the question of which separation parameters to bin in, that is, which triangle configurations to include in each bin. Nichol et al. (2006) and Kulkarni et al. (2007) measured the 3PCF in bins of s, u , and θ , that is, they counted triplets of galaxies that satisfy $s \in s_0 \pm \Delta s$, $u \in u_0 \pm \Delta u$, $\theta \in \theta_0 \pm \Delta\theta$ for the bin centered on u_0, s_0, θ_0 . In their measurement of the LRG 3PCF using the DR3 sample, Kulkarni et al. (2007) used very small resolution in $\Delta s = \pm 0.1 \text{ Mpc}$ (1% at $10 h^{-1}\text{Mpc}$) and $\Delta\theta = \pm\pi/100$, and an intermediate value for $\Delta u = \pm 0.1$. With such small resolution the result is that $Q(\theta)$ is measured with low signal-to-noise (since there are few pairs and triplets in each bin) and since Δu is not small (for $u = 2$, $s = 10$ the bin size of the second side of the triangle is 12% of the side), there are triplets counted in two or more configurations, or ‘bins’. With this binning scheme is not possible to measure the

LRG 3PCF on larger scales. But just increasing bin size in this way would lead to have very different triangles accepted in the same bin, as shown in the right side of Fig. 2.

In this work, we use the parameters s, u and θ to determine the centers of the triplet bins, but we construct the bins themselves directly in each of the pair separations, with $\Delta r_{ij} \propto r_{ij}$, i.e., we use bins of constant $\Delta \log r_{ij}$ (Marín et al. 2008; McBride et al. 2010b; McBride et al. 2010). As Fig. 2 shows, this binning scheme groups together triplet configurations that are more similar in shape (both mathematically and colloquially) and size than do bins in s, u , and θ . As a result, we can achieve either higher resolution in triangle shape and size or higher signal-to-noise for fixed resolution. Also to obtain a better signal in the 3PCF, we increase somewhat the size of the bins, which leads to a bigger correlation between the points, and therefore we do not need to measure the 3PCF for a large number of angles θ as Kulkarni et al. (2007) did.

We show in Figure 3 the results of using the different binning schemes: using the DR3 LRG sample (see §2.4 for a description of the sample), we compare the resultant 3PCF using the binning scheme used in (Kulkarni et al. 2007, in green solid lines), with the scheme used in this paper, for $\Delta r_{ij} = \pm 0.1r_{ij}$ (in open squares); it is clear that in our binning scheme $Q(\theta)$ fluctuates much less than when using the ‘old’ scheme, it reproduces better the theoretical predictions (note that there is no plateau in the new scheme that happens in the $\theta > 100$ in the $s = 10 h^{-1}\text{Mpc}$ configurations), and has smaller errors (calculated, as in Kulkarni et al. (2007), using jack-knife resampling, which will be discussed in §4).

We take advantage of this binning scheme to measure the 3PCF over a large range of triangle sizes and shapes: we study central configurations with s ranging from 7 (which allows us to compare this measurements to previous works) to $30 h^{-1}\text{Mpc}$ (on the quasi-linear regime, in order to estimate bias parameters), with $u = 2$ and 15 equally spaced values of θ . For other studies (outside the scope of this paper) such as finding best-fit galaxy population (HOD) parameters from fits to the 3PCF, it is necessary to carry out measurements on smaller scales. The results are limited by shot noise on small scales (due to the small spatial density of the LRG field) and by finite volume on large scales.

In Figure 4 we illustrate the sensitivity of the reduced 3PCF measurement to the choice of binning resolution. We show measurements with $s = 7$ and $15 h^{-1}\text{Mpc}$ for the SDSS DR7-Dim LRG sample (see §2.4). The blue dotted, solid red, and dashed magenta curves represent results with $\Delta r_{ij}/r_{ij} = \pm 0.05, 0.1$, and 0.2 , respectively. We can see significant bin-dependent differences in the reduced 3PCF amplitude, particularly for elongated triangle configurations (θ close to 0° or 180°). The differences appear to increase for larger scales. Proceeding from smaller to larger bins, the configuration-dependence of Q is smoothed out, and the measurements for different values of θ become more strongly correlated. On the other hand, the signal-to-noise for each measurement increases with bin width. We choose our binning to balance the need for a good 3PCF signal with the ability to discern shape-dependent features of the 3PCF. After

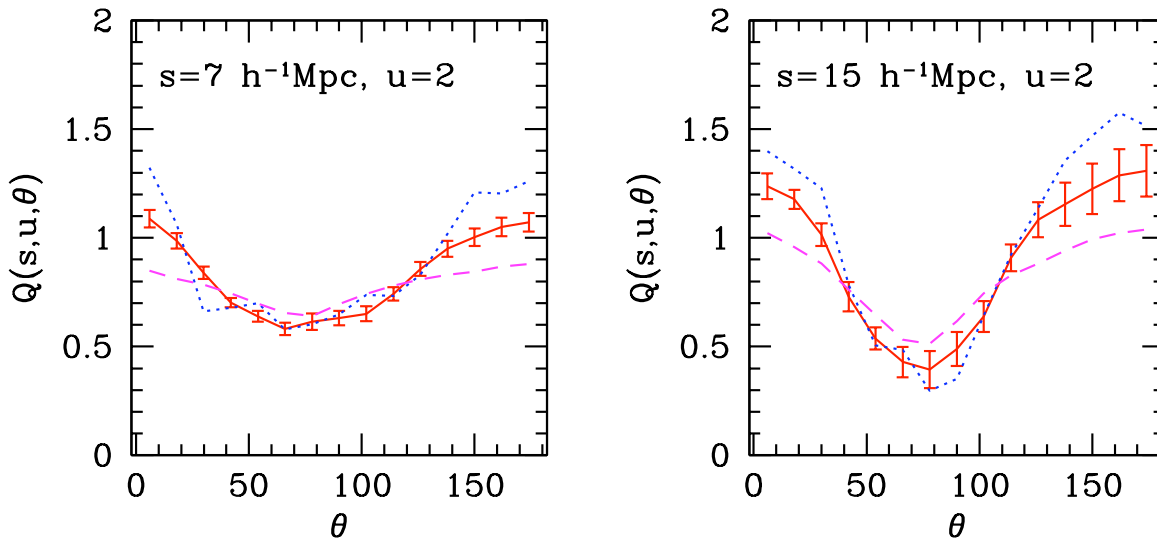


FIG. 4.— Effects of binning in the 3PCF measurement for the SDSS DR7-Dim LRG sample, for configurations with $u = 2$. Left: measurements with $s = 7 h^{-1} \text{Mpc}$. Right: $s = 15 h^{-1} \text{Mpc}$. The blue dotted, solid red, and dashed magenta curves represent results with $\Delta r_{ij}/r_{ij} = \pm 0.05, 0.1$, and 0.2 , respectively.

experimenting with simulations, we settled on a 14%, i.e. $\Delta r = \pm 0.07r$ binning resolution, for all LRG samples we studied (see §2.4).

2.3. The HOD Model

The HOD model (Jing et al. 1998; Seljak 2000; Scoccimarro et al. 2001; Berlind & Weinberg 2002; Cooray & Sheth 2002; Zheng et al. 2005, eg.) provides a parametrized prescription for the galaxy spatial distribution. The first component is a model for the distribution of dark halos. One specifies the halo mass function, $n(M)$, the spatial correlations of the halos, and the density profiles for halos of mass M , all based on analytical models and fits to N-body simulations (eg. Press & Schechter 1974; White & Rees 1978; Sheth et al. 2001; Tinker et al. 2008). The second component is the HOD itself, a model specifying how galaxies occupy dark halos as a function of halo mass.

The HOD is a parameterized model of the PDF $P(N|M)$, the probability that a halo of mass M contains N galaxies with specified properties. The mean occupation function, $\langle N(M) \rangle$, is well modeled when one separates the contribution from central galaxies, $N_{cen}(M)$, which is roughly a step function in halo mass (for halos above a certain mass M_{min}), and the contribution of the satellite galaxies, $N_{sat}(M)$, which appears to be well characterized by a power law in halo mass (Guzik & Seljak 2002; Kravtsov et al. 2004; Zheng et al. 2005) i.e., $N_{sat} \sim (M/M_1)^\alpha$, where M_1 characterizes the mass of halos that host satellite galaxies, and the exponent α describes the high-mass slope of the satellite occupation number.

There is not a unique model for the galaxy HOD; in fact there are many functional forms of $\langle N(M) \rangle$, as well as the number of parameters describing a particular HOD. Also, apart from the mean HOD, one needs to specify the higher moments of $P(N|M)$. The distributions of $N_{cen}(M)$ and $N_{sat}(M)$ are found to be consistent with nearest-integer (Bernoulli) and Poisson distributions (Kravtsov et al. 2004; Zheng et al. 2005); and the satellite galaxies are assumed to be distributed

within halos according to the NFW halo mass profiles (Navarro et al. 1997). The HOD parameters can be found using different statistics of galaxy clustering (eg. Zehavi et al. 2004, 2005b; Kulkarni et al. 2007; Blake et al. 2008; Reid & Spergel 2009; Zheng et al. 2009; Ross & Brunner 2009).

In the case of LRGs, there is consensus (eg. Kulkarni et al. 2007; Zheng et al. 2009; Sabiu et al. 2010, and references therein) that these galaxies form mostly in high-mass halos with mass $M \sim$ a few times 10^{13} to $10^{14} h^{-1} M_\odot$, while a few percent of them (in halos with $M \gtrsim 10^{14} h^{-1} M_\odot$) have to be satellites within halos in order to produce the 2PCF exhibited on smaller scales (Masjedi et al. 2006); the exact values differ depending on the statistic used and models of $\langle N(M) \rangle$ that were used. As we will see below in §2.5, the HOD model is a powerful way to create mock galaxy catalogs, and in §5.2, the HOD is also effective in modeling the non-linear and the large-scale bias.

2.4. The SDSS LRG sample

The SDSS Luminous Red Galaxies, as selected by the algorithm developed by Eisenstein et al. (2001), are an excellent tracer of dark matter on large scales due to their high luminosity, which allow us to map them up to $z \sim 0.5$ and comoving volumes up to $1.5 (h^{-1} \text{Gpc})^3$. The selection algorithm, and the high success rate of the spectroscopy makes (average sky completeness of 98%) the LRG sample nearly volume-limited up to $z \sim 0.35$ and flux limited up to $z \sim 0.47$.

We use galaxies drawn from a sample comprising 105,831 spectroscopically selected LRGs, based on SDSS Data Release 7 (DR7, Abazajian et al. 2009). The LRG galaxy selection algorithm is described in Eisenstein et al. (2001), and the DR7 LRG samples we use are drawn from the “DR7-Full” catalog described in Kazin et al. (2010), which is publicly available³. The DR7-Full sample spans the redshift range $0.16 < z < 0.47$ and includes a range of luminosities in SDSS g -band

³ <http://cosmo.nyu.edu/~eak306/SDSS-LRG.html>

TABLE 1
SDSS LRG SAMPLES USED

Sample	area	redshift	Luminosity	Number of galaxies	average density
DR7-Full ^a	7,908 deg ⁻²	0.16 < z < 0.47	-21.2 > M _g > -23.2	105,831	6.70 × 10 ⁻⁵ (h ⁻¹ Mpc) ³
DR7-Dim ^a	7,189 deg ⁻²	0.16 < z < 0.36	-21.2 > M _g > -23.2	61,899	9.40 × 10 ⁻⁵ (h ⁻¹ Mpc) ³
DR7-Bright ^a	7,189 deg ⁻²	0.16 < z < 0.45	-21.8 > M _g > -23.2	30,272	2.54 × 10 ⁻⁵ (h ⁻¹ Mpc) ³
DR3-Full ^b	3,816 deg ⁻²	0.16 < z < 0.55	-21.2 > M _g > -23.2	50,987	6.50 × 10 ⁻⁵ (h ⁻¹ Mpc) ³

^afrom Kazin et al. (2010)

^bfrom Eisenstein et al. (2005)

of $-23.2 < M_g < -21.2$, where the magnitudes have been K-corrected and passively evolved to $z = 0.3$, near the median redshift of the sample. The sample is nearly volume-limited for redshifts $z \lesssim 0.36$ and drops off due to the flux limit at higher redshift. The sample covers a sky area of 7908 deg² (close to 20% of the sky) and includes data from both the northern and southern Galactic hemispheres.

From this main catalog, two important samples are extracted: one that includes all LRGs, but is volume-limited, which we call “DR7-Dim”, which has a maximum redshift of $z = 0.36$ and median spatial density of $\sim 10^{-4}$ (h⁻¹Mpc)⁻³, and a sample of the bright LRGs, where $M_g < -21.8$, which we call “DR7-Bright”, which reaches redshifts up to $z = 0.44$ and has a low spatial density $\sim 2.5 \times 10^{-5}$ (h⁻¹Mpc)⁻³. Both of these samples are the same as the ones presented in Kazin et al. (2010), and use data from the northern cap only, in order to have more mock catalogs when estimating the errors and covariance of our measurements (see §2.5 for more details).

To calculate the correlation functions, we use the same DR7-Full random catalogs as in Kazin et al. 2010, which contain 10 times the number of LRGs as the data. These random catalogs have been built having the same redshift selection function as the data, as well as the same sky completeness. For the purposes of calculating the 3PCF in a reasonable time, on the largest scales we lower the number of random points; when measuring the 3PCF at $s = 30$ h⁻¹Mpc, our largest scale, our random catalog has 4 times the number of data points.

For comparison, we have also analyzed the earlier SDSS DR3 LRG sample used by Kulkarni et al. 2007. That sample covers 3816 deg² and contains 50,967 LRGs spanning the redshift range $0.15 < z < 0.55$. In this case, we use the data and random catalogs of Eisenstein et al. (2005), kindly provided by the author.

The information on these samples is summarized in Table 1.

The LRGs, i.e., giant red ellipticals, are associated with massive halos, and they are highly clustered (see for instance Zehavi et al. 2005a; Masjedi et al. 2006). This is illustrated in Figure 5, where we show the redshift space 2PCF of the DR7-Dim and DR7-Bright LRGs, along with the dark matter redshift 2PCF from N-body simulations with a cosmological parameters based on the WMAP5 results (Komatsu et al. 2009, described in §2.5). Both LRG samples have a higher 2PCF than the dark matter, and on large scales the offset seems constant, and due to this fact we can say that the LRGs are a biased tracer of dark matter on large scales. The DR7-Bright LRGs have a higher 2PCF than the DR7-Dim

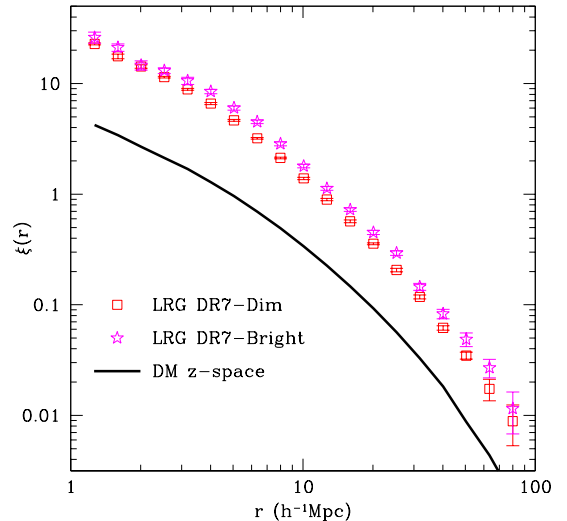


FIG. 5.— The redshift space 2PCF for LRGs. Red open squares correspond to measurements in the DR7-Dim LRG sample, magenta stars represent the 2PCF of the DR7-Bright LRG sample. Thick black solid line corresponds to the dark matter 2PCF, from N-body simulations by Sabiu et al. (2010). Errors from the variance of LasDamas LRG mock catalogs.

LRGs, suggesting that they are associated with more massive halos (Zheng et al. 2009).

2.5. Simulations & Mock catalogs

To help analyze and interpret the 3PCF results, we use mock catalogs drawn from N-body simulations. The mock catalogs serve two functions: (i) to measure the 3PCF of dark matter, with which the galaxy 3PCF measurements can be compared to infer the bias, and (ii) to determine the expected error covariance matrix for the 3PCF from the variance among a large number of mock catalogs. We use different simulations tailored to these different functions.

First, to study the dark matter two- and three-point correlation functions, we use six N-body simulations carried out by Sabiu et al. (2010), kindly provided by the author, using the GADGET code. The cosmological model is a spatially flat Λ CDM universe, with matter density parameter $\Omega_m = 0.27$, baryon density $\Omega_b = 0.045$, power spectrum amplitude $\sigma_8 = 0.8$, reduced Hubble parameter $h = 0.7$, and initial power spectrum index $n_s = 0.95$. The simulation box volume is 1 (h⁻¹Gpc)³ and contains 512³ dark matter particles with a particle mass of 5×10^{11} h⁻¹M_⊙, with a spatial softening of 60 h⁻¹kpc, and we use the output at $z = 0.3$, the mean redshift of the LRGs, to compare their correlation functions.

Since using all the dark matter particles for the 3PCF

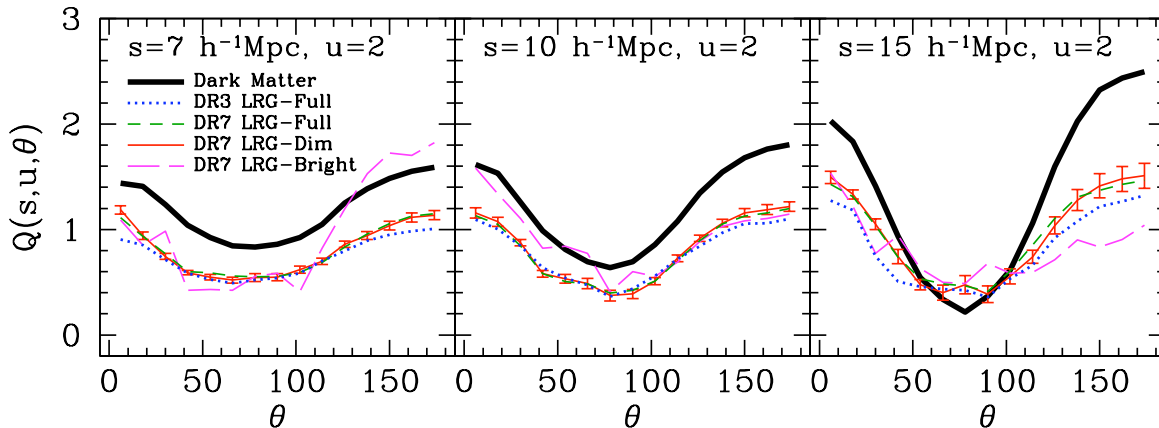


FIG. 6.— The redshift-space, reduced LRG 3PCF, $Q(\theta)$, for configurations with $u = 2$ and $s = 7$ (left), 10 (middle), and 15 (right) $h^{-1}\text{Mpc}$. *Red solid line*: DR7-Dim LRG sample, errors from variance of LasDamas mock catalogs. *Green short-dashed line*: DR7-Full LRG sample. *Magenta long-dashed line*: DR7-Bright LRG sample. *Blue dotted line*: DR3-Full LRG sample. *Thick black line*: Dark Matter 3PCF from simulations. Error bars from the variance of LasDamas LRG mock catalogs.

calculations would take a prohibitively long time, we randomly select particles from the simulation, to a degree where we are sure that the dilution will not affect the results. For the 3PCF measurement, this depends on scale, and we use between 5% and 0.5% of the particles (a higher fraction for smaller scales). To obtain the spatial coordinates in the redshift-space dark-matter catalog, we use the long-distance approximation in the z -direction (see e.g. Bernardeau et al. 2002) to account for the effect of peculiar velocities on the measurement of the correlation functions.

We use the dark matter halo catalogs obtained from these simulations to study redshift distortions in the estimation of the bias parameters (section §5.2 below), found using a Friends-of-Friends algorithm (Davis et al. 1985) with a linking length of $b = 0.2$ times the mean interparticle separation. To populate halos with mock LRGs, we use the best-fit HOD parameters from fits to the projected 2PCF by (Zheng et al. 2009) in their 5-parameter model. We assign mock galaxy positions, based on halo profiles, and peculiar velocities (based on a gaussian distribution, which depends on the mass of the host halo) of galaxies inside halos using a code kindly provided by Jeremy Tinker.

Second, to estimate the errors in the 3PCF estimates, we use the covariance among public mock catalogs from the LasDamas simulations (McBride et al. 2010b)⁴. As will be discussed in §4, we prefer this error estimation method to the use of jack-knife (JK) resampling. For the LasDamas simulations, the cosmological model is similar but not identical to that above: flat, ΛCDM with $\Omega_m = 0.25$, $\Omega_b = 0.04$, $\sigma_8 = 0.8$, $h = 0.7$, and $n_s = 1$. For this set of parameters, the LasDamas team has carried out N-body simulations in boxes of different sizes to model galaxies of different luminosities; for the LRGs, they use 40 boxes with volume of $2400^3 (h^{-1}\text{Mpc})^3$, each one containing 1280^3 dark matter particles with a particle mass of $4.57 \times 10^{11} h^{-1}M_\odot$.

These simulations are used to construct mock galaxy catalogs by placing galaxies in dark matter halos using a Halo Occupation Distribution (HOD) model (Berlind & Weinberg 2002), with HOD parameters fit

from the observed SDSS LRG 2-point clustering. From this main set they create two types of galaxy mock catalogs, one that resembles the LRG DR7-Dim catalog, with $z_{max} = 0.36$, and one set that resembles the Bright LRG sample with $z_{max} = 0.44$. The mocks reproduce the SDSS DR7 geometry, and they include redshift-space distortions from peculiar velocities. These galaxy mocks have been shown to reproduce well the form of the DR7 LRG 2PCF on large scales (Kazin et al. 2010), and we show below that they are in general agreement with the 3PCF measurements as well. Since our DR7-Dim and DR7-Bright samples use only the northern cap of the SDSS, in each LasDamas box it is possible to extract four mock LRG catalogs; in this way, we have 160 mock catalogs for each sample.

3. RESULTS

We present the redshift-space LRG 3PCF measurements in Figures 6-7 for configurations with s between 7, and $30 h^{-1}\text{Mpc}$, with $u = r_2/r_1 = 2$. We chose these scales, which go from the mildly non-linear to the quasi-linear regime, in order to calculate the large-scale bias of LRGs, and use only triangles with $u = 2$ since that puts all triplet distances (i.e. the sides of the triangle) above the s selected. If we used $u = 1$, then our most collapsed triangles would have been in the strong non-linear regime, affecting our bias estimates. We could also try triangles with $u = 3$ or more, but then our biggest distances would be comparable to the scale of the survey, and also computing the 3PCF becomes prohibitive. We first discuss the measurements on intermediate and large scales and then explore the 3PCF error estimates.

3.1. LRG 3PCF on intermediate scales

Figure 6 shows the reduced 3PCF of the DR7 LRG samples on intermediate scales, for $s = 7, 10$, and $15 h^{-1}\text{Mpc}$. For clarity, we show diagonal error bars only for the DR7-Dim sample, calculating using the 3PCF variance between the LasDamas mocks. For comparison, we also show the 3PCF for the DR3 LRG sample. The solid black curves show the 3PCF of the dark matter from the N-body simulations.

The reduced 3PCF shows the general shape-dependence expected from gravitational instability theory (Bernardeau et al. 2002): the amplitude is higher

⁴ <http://lss.phy.vanderbilt.edu/lasdama/>

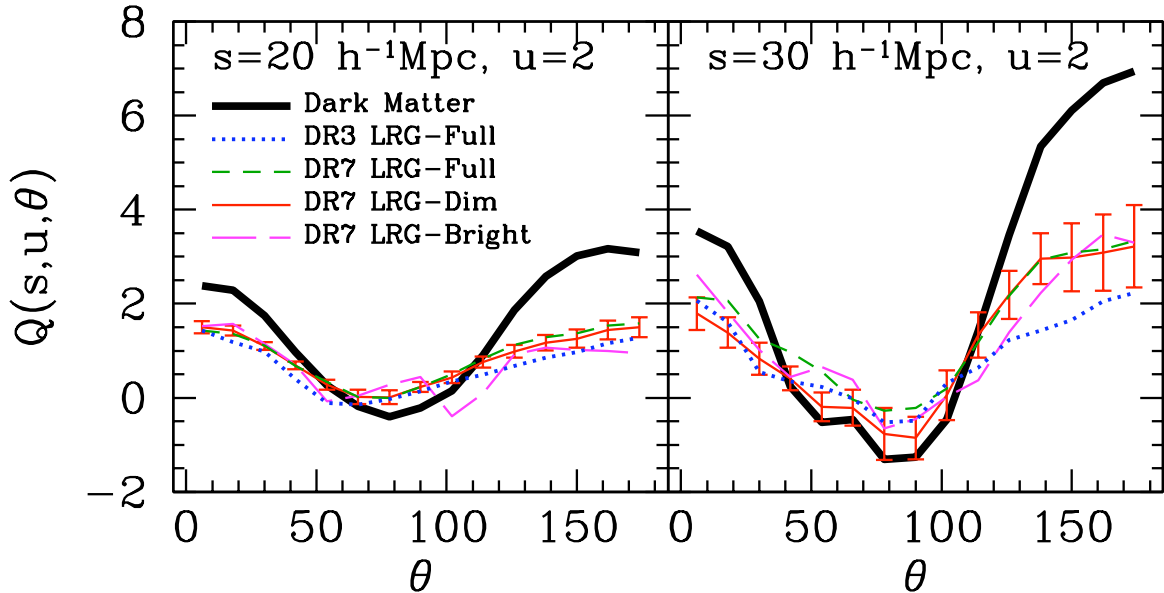


FIG. 7.— The redshift-space, reduced LRG 3PCF, $Q(\theta)$, for configurations with $u = 2$ and $s = 20$ (left) and 30 (right) $h^{-1}\text{Mpc}$. *Red solid line*: DR7-Dim LRG sample, errors from variance of LasDamas mock catalogs. *Green short-dashed line*: DR7-Full LRG sample. *Magenta long-dashed line*: DR7-Bright LRG sample. *Blue dotted line*: DR3-Full LRG sample. *Thick black line*: Dark Matter 3PCF from simulations. Errors from the variance of LasDamas LRG mock catalogs. Note difference in vertical scale compared to Figure 6.

for elongated triangle configurations ($\theta \sim 0^\circ, 180^\circ$), reflecting anisotropic velocity flows along density gradients. The configuration dependence is less pronounced on smaller scales, where quasi-virialized, more isotropic flows and structures dominate. Since these measurements are in redshift space, the configuration dependence also reflects the effects of redshift distortions due to peculiar velocities.

Since LRGs are biased tracers of the dark matter, the 3PCF of the LRGs differs from that predicted for the dark matter. On small scales, the reduced 3PCF amplitude of the LRGs is smaller by a nearly constant factor from that of the dark matter. On larger scales, the nature of the 3PCF bias changes: there is a shape dependence in the offset between the LRG and dark matter amplitudes, with the galaxy 3PCF showing less configuration dependence than that of the dark matter.

Comparing the DR7-Full results to the DR3 measurements, which cover half the volume of the DR7 sample, we find general consistency in the 3PCF amplitude on these intermediate scales. For $s = 15 h^{-1}\text{Mpc}$, the DR3 amplitude is slightly lower than that of the DR7 sample for all configurations; this is a consequence of the smaller volume sampled to estimate the correlation functions: as observed in other studies (see Marín et al. 2008, and refs. therein), the 3PCF is more sensitive to the sample volume than the 2PCF.

In general, there are no important differences between the DR7-Full and the volume-limited DR7-Dim sample results. There are differences between these and the DR7-Bright sample: the reduced 3PCF for the bright LRGs fluctuates much more and it deviates from the DR7-Dim sample results for the elongated triangles (large θ) for the $s = 7$ and $15 h^{-1}\text{Mpc}$ configurations, and in the collapsed triangles (small θ) for the $s = 10 h^{-1}\text{Mpc}$ configurations. Since we have used a binning more tailored to measure the DR7-Dim correlations on the DR7-Bright (a much less dense sample) measurements, we ex-

pect more fluctuations due to poorer statistics and effects of large structures (Nichol et al. 2006); we’ll explore the variance of bright LRGs in §3.3 below.

3.2. LRG 3PCF on large scales

In Figure 7 we show the reduced 3PCF for LRGs on large scales, for $s = 20$ and $30 h^{-1}\text{Mpc}$, with $u = 2.0$. As expected from 2nd-order perturbation theory, the reduced 3PCF shows a stronger configuration-dependence on these scales compared to smaller scales, with a dramatic increase in the difference in amplitude between elongated and rectangular configurations at $s \geq 20 h^{-1}\text{Mpc}$. That behavior is seen for both the dark matter and the LRG samples. For $s = 30 h^{-1}\text{Mpc}$, the LRG 3PCF dependence in θ is more asymmetrical between collapsed and elongated configurations, as it happens with the dark matter 3PCF. The errors are greatly increased as well, and there are strong anticorrelations, i.e. negative values of $Q(\theta)$, for the rectangular configurations; this is again a consequence of the filamentary shape of the large-scale structure.

The large scale 3PCF of the DR7-Bright galaxies is similar to the DR7-Dim 3PCF, with less significant fluctuations on larger scales. On these scales the finite-volume effects can be observed more clearly in the 3PCF: comparing the DR7-Full and DR7-Dim LRG samples, we can see that in general they agree within the errorbars, and the small differences are due to a combination of finite-volume effects and biasing effects (the DR7-Full sample includes brighter galaxies at large redshifts, which have a different clustering bias than the DR7-Dim sample). Comparing the DR3-Full results compared to DR7-Full and even DR7-Dim, we can see that the DR3-Full 3PCF deviates from the DR7 samples on the elongated configurations (larger scales).

3.3. Comparison with LasDamas mocks

In Figure 8 we compare the 3PCF measurements for the DR7 LRGs, as shown previously in §3.1 and §3.2

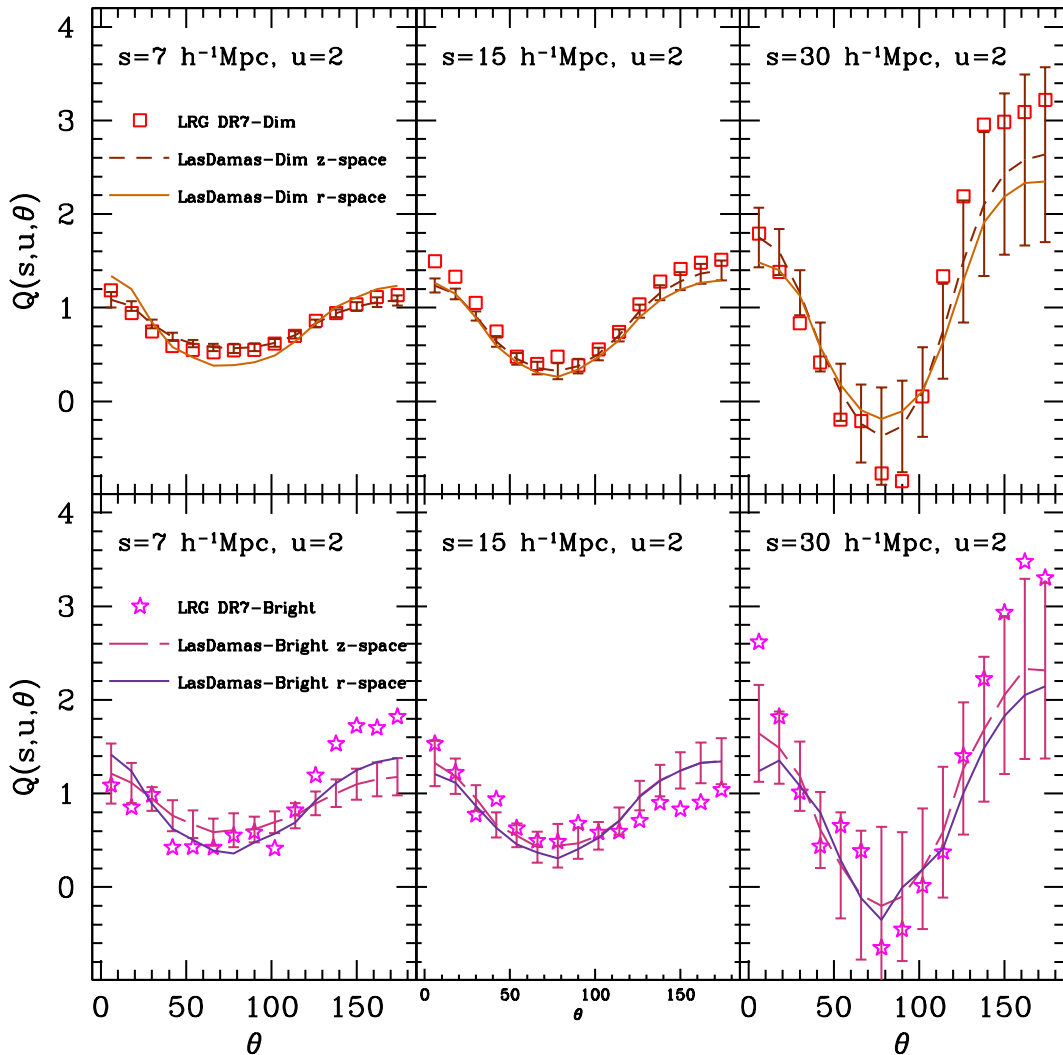


FIG. 8.— Comparison of LRG 3PCF with LasDamas mocks measurements. Symbols represent DR7 measurements, solid lines represent the mean of the 3PCF measured in real-space LasDamas catalog, dashed lines represent the mean of the 3PCF measured on redshift-space mocks. Error bars represent the variance of the redshift-space 3PCF measured in 160 mocks.

to the ones obtained from the LasDamas mocks, with dashed lines for redshift-space measurements, solid lines for real-space measurements. Here we present a representative set of values, with $s = 7, 15, \text{ and } 30 h^{-1}\text{Mpc}$. In the top panels we show the comparison for DR7-Dim galaxies; in general the agreement is good, and usually within the $1\text{-}\sigma$ error bars.

In the lower panels, we compare DR7-Bright galaxies and the mock 3PCFs. It can be seen that the variance of the bright mocks is larger compared to the dim ones, and the agreement between the mocks and the data is not as good, especially on smaller scales for the elongated configurations. Although due to their low density less signal-to-noise and more fluctuations in $Q(\theta)$ are expected, the variance from the mocks should reflect this, and that is not the case for the smaller scales. Since the mocks are built in order to fit the measured 2-point statistics, it can happen that the mock miss the higher-order statistics, and for future modeling these statistics have to be

considered.

Note also the differences between the real and redshift space measurements in the LasDamas mocks. Both have a dependence on shape, but on small scales the real space 3PCF has a more pronounced shape dependence. On bigger scales, especially around $s = 15 h^{-1}\text{Mpc}$, they are very similar within the errors. Comparing these differences to the ones found by Marín et al. (2008), there are two causes of this: first, the LRGs are galaxies that inhabit massive halos (eg. Kulkarni et al. 2007; Zheng et al. 2009, among others), which are in the center of the gravitational potential wells of the large matter structures, and therefore they are less affected peculiar velocities. Second, the 3PCF on larger scales is much more affected by the morphology of the structures than from the peculiar velocities, and therefore on the largest scales the distortions of the reduced 3PCF will be smaller than on the small scales. There is also a resolution (or binning) component to this; in very thin bins we might

be able to detect better the distortions on large scales. We will use this similarity between the real and redshift space 3PCF below in §5.2 to estimate real-space bias parameters from the 3PCF.

4. 3PCF ERROR ESTIMATES

Two methods have been commonly employed to estimate errors in clustering measurements: the variance among mock samples and jack-knife (JK) sampling. Zehavi et al. (2005b) showed that the JK method can be reliable for obtaining the covariance matrix in the 2PCF, comparing with mock catalogs from independent realizations. In principle, the errors on the 3PCF depend on higher-order correlations up to sixth order (see, e.g., Szapudi 2005) and could be calculated analytically once the latter are measured. In practice, including edge effects and shot noise contributions makes the analytic computation of these errors a complicated and computationally challenging problem. The jack-knife, in which one sequentially removes subvolumes and computes the variance among 3PCF measurements for the remaining volumes, provides a convenient computational short-cut, but there is no fundamental basis for assuming it is accurate in this context. Indeed, the jack-knife method assumes that the removed subvolumes are independent, ignoring density perturbation modes on scales larger than those of the subvolumes. The variance in 3PCF estimates among a large number of simulated realizations of a given model (mock samples) provides a ground-truth measure of the 3PCF error for that model. If the model provides an accurate representation of the actual galaxy clustering, then the mock sample variance should provide the best estimate of the errors. In the following, we compute and compare the mock variance estimates of 3PCF errors, using the 160 LRG-Dim mocks from the LasDamas simulations, to the jack-knife variance estimations from a representative LasDamas LRG-Dim mock. In this case we divided the mock catalog into many angular regions with equal number of galaxies (at the limit of large number of subsamples, this is equivalent to have regions with equal volume); each JK subsample is built by extracting one of these regions from the LRG mock.

4.1. Diagonal Errors

For the jack-knife and variance methods, the diagonal errors are given by

$$\sigma_Q^2 = \frac{E_{method}}{N} \sum_{i=0}^N (Q_i - \bar{Q})^2. \quad (7)$$

For the jack-knife method, $N = N_{JK}$, the number of subvolumes, and $E_{JK} = N_{JK} - 1$; for the variance among mocks, N is the number of independent realizations, and $E_{var} = 1$.

To have a qualitative estimate of the differences in the diagonal errors between the two methods, we calculate, for each sample, the average of the reduced 3PCF for all angles in a particular configuration, i.e., we calculate $\bar{Q}(s = 15, u = 2, \theta)$, the mean of $Q(\theta)$ for triangles with $s = 15.0 \ h^{-1}\text{Mpc}$, $u = 2.0$, as a function of the number N of samples. We do this for three values of theta, one corresponding to an almost collapsed triangle ($\theta = 18^\circ$), another for a rectangular configuration

($\theta = 90^\circ$), and one for an almost completely extended configuration ($\theta = 160^\circ$). We chose this scale since the 3PCF here is well behaved and does not have big diagonal errors, but also is large enough to make visible the effects of the JK resampling in the 3PCF (i.e. test the ‘independent regions’ hypothesis).

The results are shown in Figure 9. In the left panel, we compare $\bar{Q}(s = 15, u = 2, \theta)$ for mocks and for JK subsamples. The average values converge very fast with N , and the fact that the means of the jack-knife samples and the mocks are close to each other (differences at the level of 5% on these scales) is a good signal that we can use the mocks for the covariance measurements. In the right panel we show the variance (standard deviation) of $Q(s, u, \theta)$ as a function of N , for the different methods. We notice that while the mock’s variance seems to converge at large N , the JK errors tend to increase.

4.2. Covariance matrices

For N -point correlation functions, measurements for different configurations are strongly correlated, therefore the off-diagonal errors must be included in model-fitting and parameter estimation. Figure 10 shows the correlation matrices of the 3PCF for configurations with $s = 15 \ h^{-1}\text{Mpc}$, $u = 2$, and varying θ , comparing the jack-knife (top row) and mock-covariance methods (middle row), for different numbers of jack-knife sub-volumes and mock realizations. For both methods, the off-diagonal correlation coefficients increase with increasing N , which goes from 10 to 160 subsamples/realizations.

For these configurations, the off-diagonal terms tend to converge when $N \geq 40$. As can be seen in the bottom row of Figure 10, where we show the ratio between the off-diagonal terms of the covariance matrices, $|C_{ij}^{mocks}(N)/C_{ij}^{JK}(N)|$, both methods yield similar results except for the terms relating very collapsed and very elongated configurations, where the jack-knife configurations have higher correlations. This enhanced covariance for the JK methods is due to the fact that this method uses only one ‘realization’; while on small scales the regions can be effectively independent, on large scales (i.e., when examining large triangles) these regions are correlated, and then the JK assumption breaks down.

Even though for large N the covariance matrix converges for the JK method, and we would be able to extract more information from the covariance matrix, we would be introducing artificial correlations since the bigger N is, the smaller and ‘less independent’ the volumes of the subsamples are. In our analysis of large-scale clustering (for bias and cosmological parameters) we will use the 3PCF error covariance matrices from the variation among the 160 mock catalogs.

5. LRG BIAS

In the following we quantify the differences between dark matter and LRG clustering, known as galaxy biasing. As we have seen above, there are important differences between them, and, in a similar fashion to what can be done from 2-point correlations, we would like to measure the bias of the LRG 3PCF to obtain cosmological information. One way to relate dark matter and galaxy clustering in real space is to adopt a deterministic and local bias model (e.g. Fry & Gaztanaga 1993; Frieman & Gaztanaga 1994),

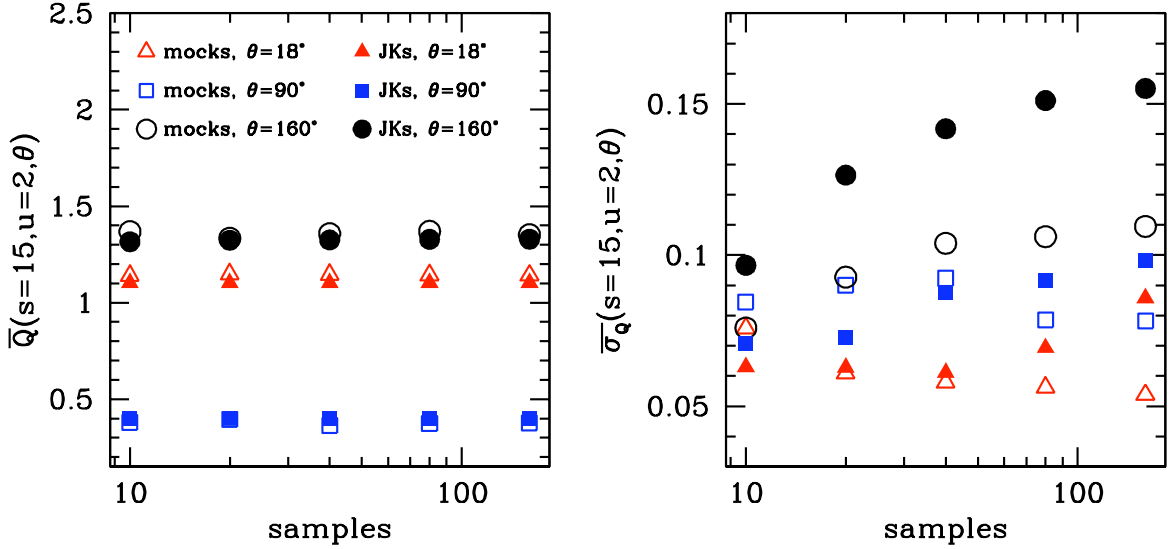


FIG. 9.— Comparison of mean (left) and standard deviation (right) of different reduced 3PCF as a function of the number of samples, for different configurations. Left: $\bar{Q}(s=15, u=2, \theta)$, the mean of the $Q(s, u, \theta)$ as a function of number of samples, using LasDamas mocks (open symbols) or jack-knife subsamples, for triangles with $s = 15 h^{-1}\text{Mpc}$ and $u = 2$, and $\theta = 18^\circ$ (triangles), $\theta = 90^\circ$ (squares), and $\theta = 160^\circ$ (circles) Right: $\bar{\sigma}_Q$, the standard deviation of $Q(\theta)$ as a function of subsamples, from eq. (7).

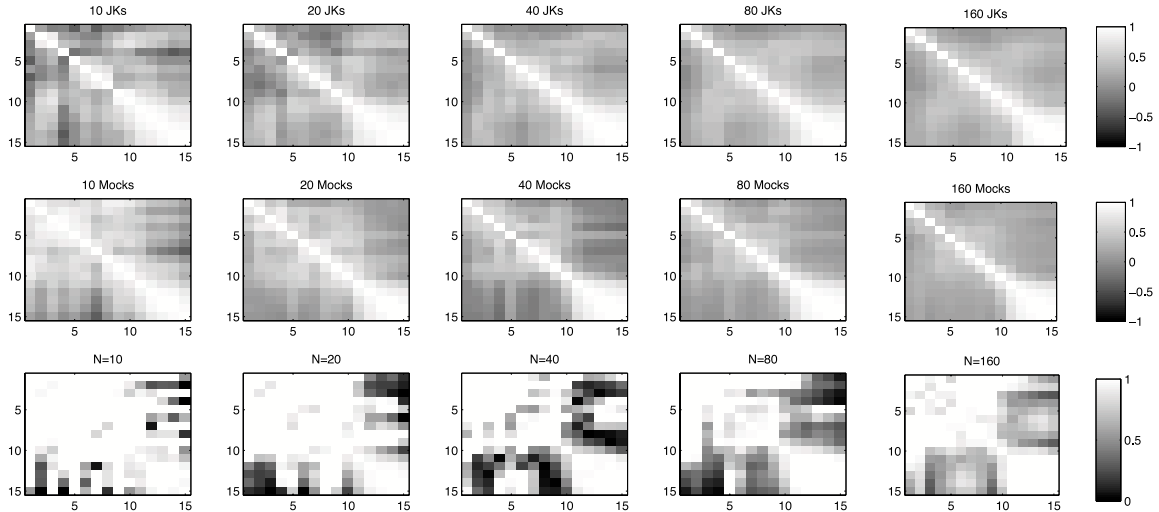


FIG. 10.— Normalized correlation matrices for the reduced, redshift-space 3PCF $Q(s = 15h^{-1}\text{Mpc}, u = 2.0, \theta)$ measured in LasDamas mock catalogs, using jack-knife resampling for one LasDamas LRG-Dim mock (top), and the covariance of mocks from independent realizations (middle), for $N = 10, 20, 40, 80, 160$. The bottom row shows the ratio of each matrix element $|C_{ij}^{\text{mocks}}(N)/C_{ij}^{\text{JK}}(N)|$. Each matrix element i, j corresponds to the correlation coefficient of $Q(\theta = \pi/30 + \pi * (i - 1)/15)$ and $Q(\theta = \pi/30 + \pi * (j - 1)/15)$

$$\delta_{gal} = f(\delta_{dm}) = b_1 \delta_{dm} + \frac{b_2}{2} \delta_{dm}^2 + \dots, \quad (8)$$

where δ_{gal} and δ_{dm} are the local galaxy and dark matter overdensities smoothed over some scale R . To leading order, this bias prescription leads to a relation between the galaxy and dark matter reduced 2PCF and connected 3PCF amplitudes,

$$\begin{aligned} \xi_{gal}(r) &\approx b_1^2 \xi_{dm}(r) \\ \zeta_{gal}(r_{12}, r_{23}, r_{31}) &\approx b_1^3 \zeta_{dm}(r_{12}, r_{23}, r_{31}) + \\ &\quad b_2 b_1^2 [\xi_{dm}(r_{12}) \xi_{dm}(r_{23}) + \text{perm.}] \end{aligned} \quad (9)$$

In addition to the bias, the 3PCF can help breaking the degeneracy between the bias and the r.m.s variance in

density of spheres with radius $R = 8 h^{-1}\text{Mpc}$, σ_8 . This parameter is related to the overall amplitude of the dark matter 2PCF. If we use the 2PCF in equation (9), adopting a fiducial σ_8^{fid} , then there is a degeneracy between σ_8 and b_1 in linear theory (Pan & Szapudi 2005);

$$\xi_{gal} = b_1^2 \left(\frac{\sigma_8}{\sigma_8^{fid}} \right)^2 \xi_{dm, \sigma_8^{fid}}, \quad (11)$$

For the 3PCF, there is a factor $(\sigma_8/\sigma_8^{fid})^4$ that needs to be multiplied the right side of eq. (10). To find the best-fit for the bias parameters and σ_8 , we use dark matter correlations in a particular fiducial cosmology, and we use equation (11) for the 2PCF fit; for the reduced 3PCF, in

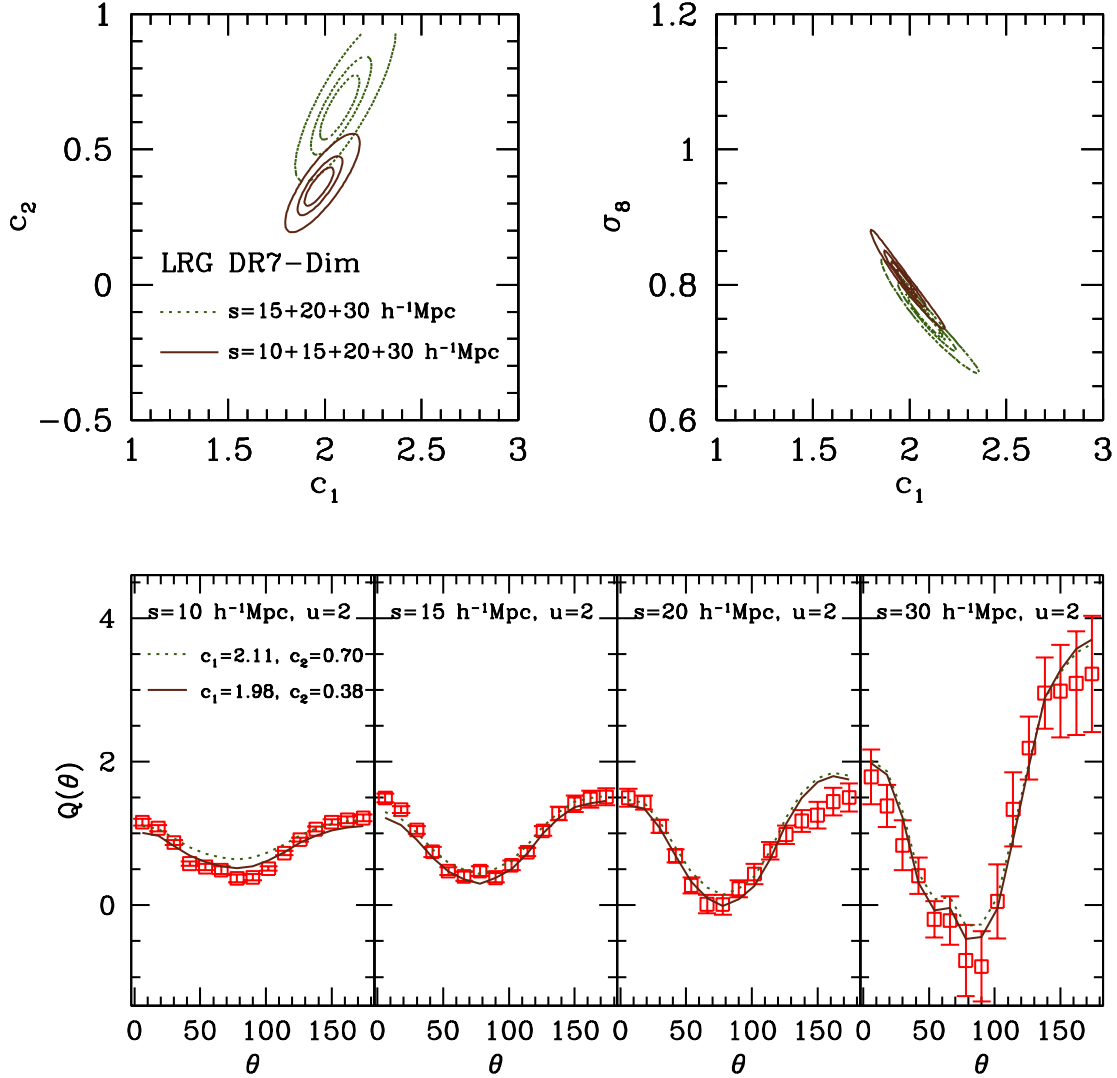


FIG. 11.— Best-fit marginalized likelihood of bias parameters and σ_8 from the 2PCF and 3PCF using the LRG DR7-Dim sample. On the top plots, contours represent $\Delta\chi^2 = 1.0, 2.3$ and 6.2 . On the bottom plots, LRG DR7-Dim 3PCF in symbols and lines represent biased dark matter 3PCF values see best-fit parameters in Table 3

this prescription reads

$$Q_{gal} = \frac{1}{c_1} (Q_{dm} + c_2) \quad (12)$$

where $c_1 = b_1$ and $c_2 = b_2/b_1$, where the dependence on σ_8 cancels, thus allowing us to break the degeneracy between b_1 and σ_8 from the 2PCF. We have to remember, however, that these approximations and expansions are applicable only on large scales and in real space, whereas our measurements are made in redshift space, where correlations are distorted due to peculiar velocities. Therefore, we have to test the validity of these formulas, and try to quantify their effects on the scales we are using for these comparisons. We will test how well this bias prescription captures the clustering statistics by fitting these relations to the dark matter and galaxy 2- and 3-point correlation functions.

5.1. Constraints on bias parameters and σ_8 in redshift space

We compare the dark matter (from the N-body simulations described in 2.5) and LRG 2PCF and 3PCF in order to constrain bias parameters using the relations (11) and (12), in this case assuming these relations are valid in redshift space, i.e. $\xi^{r\text{-space}} \rightarrow \xi^{z\text{-space}}$ and $Q^{r\text{-space}} \rightarrow Q^{z\text{-space}}$. We use all configurations with $s \geq 10 h^{-1}\text{Mpc}$, and $s \geq 15 h^{-1}\text{Mpc}$ with $u = 2$ to measure the joint likelihood of the bias parameters and σ_8 .

As described by Gaztañaga & Scoccimarro (2005) and used in Gaztañaga et al. (2005) and Marín et al. (2008), we minimize

$$\chi^2 = \sum_{i=1}^{i=2N_b} \sum_{j=1}^{j=2N_b} \Delta_i C_{ij,SV D}^{-1} \Delta_j \quad (13)$$

where N_b is the number of configurations used ($N_b =$

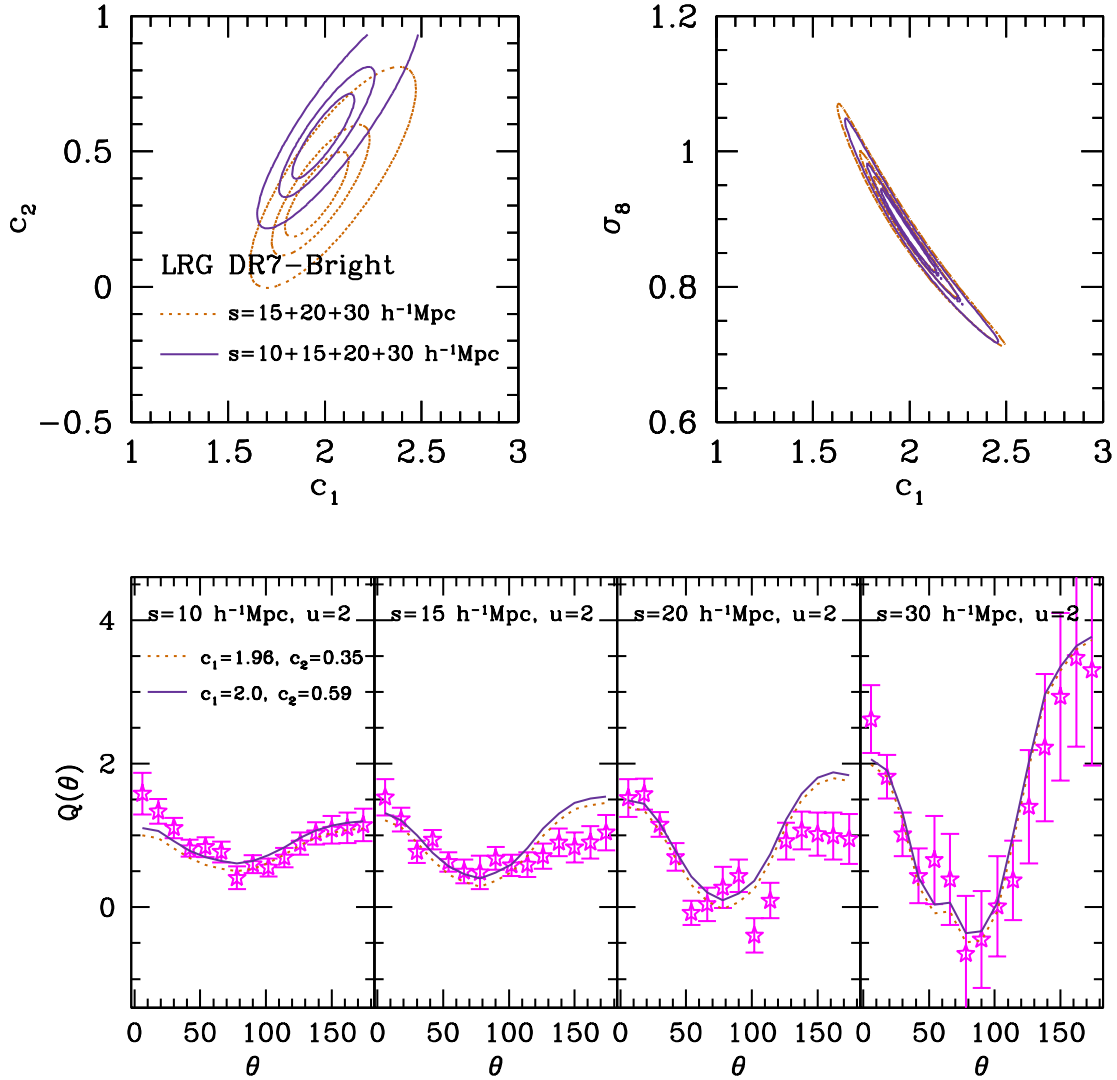


FIG. 12.— Best-fit marginalized likelihood of bias parameters and σ_8 from the 2PCF and 3PCF using the LRG DR7-Bright sample. On the top plots, contours represent $\Delta\chi^2 = 1.0, 2.3$ and 6.2 . On the bottom plots, LRG DR7-Bright 3PCF in symbols and lines represent biased dark matter 3PCF values see best-fit parameters in Table 3

60 for triangles with $s \geq 10 h^{-1}\text{Mpc}$ and $N_b = 45$ for triangles with $s \geq 15 h^{-1}\text{Mpc}$). Since we use both 2- and 3-point correlations we have

$$\Delta_i = (\xi(r_3)_i^{obs} - \xi(r_3)_i^{model}) / \sigma_{\xi(r_3)_i}, \text{ for } i \leq N_b \quad (14)$$

$$\Delta_i = (Q_i^{obs} - Q_i^{model}) / \sigma_{Q(i)}, \text{ for } i > N_b \quad (15)$$

where $\xi(r_3)^{model}$ and Q^{model} are given by eqs. (9) and (12) for the galaxies. The matrix $C_{ij,SV D}$ is the normalized covariance matrix, recalculated with the highest modes from a Singular Value Decomposition. This covariance matrix is calculated from the LasDamas LRG mock catalogs; $\sigma_{\xi(r_3)_i}$ and $\sigma_{Q(i)}$ are the uncertainties in $\xi(r_3)_i$ and $Q(i)$, respectively, and we will assign them the error bars from the mocks. We follow the suggestion of Gaztañaga & Scoccimarro (2005) and use configurations where the eigenvalues $\lambda < \sqrt{2/N_b}$. As mentioned above, we actually are more limited by the number of mocks that we use: we have to use a number of modes smaller

than the number of mocks.

The results are shown in Figures 11 and 12, where we use the covariance matrix from the 160 LasDamas mocks for each sample to constrain c_1 , c_2 , and σ_8 . In Figure 11 we show the results for the DR7-Dim sample, and in Figure 12, the results for the DR7-Bright sample. On the top panels of each figure we show constraints on the bias parameters and σ_8 , for two sets of configurations: solid lines use triangles with $s \geq 10 h^{-1}\text{Mpc}$ and dotted lines use only the largest triangles $s \geq 15 h^{-1}\text{Mpc}$. The contours correspond to $\Delta\chi^2 = 1.0, 2.3$ and 6.2 (corresponding to 1σ limits for 1-parameter fit, 1σ limit for 2 parameter-fit, and 2σ limit for 2 parameters, respectively).

We can see that in both samples a zero non-linear bias is excluded at 2σ significance. We can see that, as expected, DR7-Dim galaxies have a lower linear bias c_1 than the DR7-Bright, and there is a bigger difference in the non-linear bias parameter c_2 . Using different sets of triangles changes the results affects the area of the con-

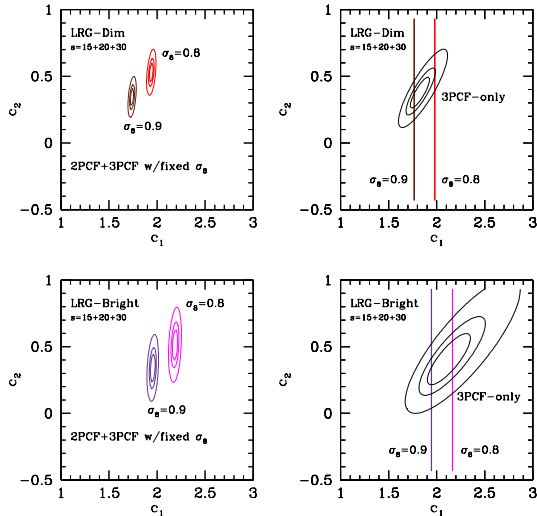


FIG. 13.— Best-fit bias parameter constraints using correlation functions separately and with fixed σ_8 . Left plots show bias constraints using the 2PCF and 3PCF when fixing σ_8 , right plots show in solid straight lines, the best fit for c_1 using only the 2PCF when σ_8 is fixed, and the ellipses show constraints in c_1 and c_2 using the 3PCF only. Upper panels shows the constraints for the DR7-Dim sample. Lower panels show constraints for the DR7-Bright sample. Contour lines represent $\Delta\chi^2 = 1.0, 2.3$ and 6.2

fidence contours, but also the best-fit results; going to smaller scales put us in the direction of the non-linear regime, where the relations in eqs. (11) and (12) are not longer valid. Observe that the error bars are not small: this is an effect of using a large number of configurations when we have a limited number of realizations (this makes the inverse of the covariance matrix highly singular, therefore we are obligated to cut many modes), and also that our errors increase on large scales.

With respect to the constraints on σ_8 , in general they agree with the WMAP5 results (Komatsu et al. 2009), but they are more dependent on which configurations are used.

The best fit values and $1\text{-}\sigma$ errors are also presented in Table 3.

In the lower two panels we show the LRG 3PCF along with the Dark Matter biased 3PCF, using the best-fit bias values mentioned above. For the DR7-Dim sample the fits are quite good, and there are not significant differences between the fits from using different triangles (solid line corresponds to fit using $s \geq 10 h^{-1}\text{Mpc}$ triangles whereas dotted lines use only $s \geq 15 h^{-1}\text{Mpc}$ triangles). For the brighter sample, the fits are less good for configurations with $\theta > 100^\circ$ deg.

We explore how the constraints on the bias parameters change if σ_8 is fixed (instead of being marginalized), and compare results to the analytical bias prediction from the HOD models. In Figure 13 we show these results, using only $s \geq 15 h^{-1}\text{Mpc}$ configurations. On the left side, the vertical ellipses correspond to constraints on the bias parameters using both the 2PCF and 3PCF, using a model where σ_8 is fixed. As expected, a lower σ_8 means a higher c_1 . The constraints on c_1 are tight, due to the lower errors in ξ , leaving mostly the uncertainty on $c_2 = b_2/b_1$.

We compare these bias parameters with that expected

from the analytical predictions from the best-fit HOD from (Zheng et al. 2009, using projected 2PCF only) for both linear and nonlinear bias in the last row of Table 3, and we have good agreement. Our error bars, in the case of $\sigma_8 = 0.8$, confirm that a zero non-linear bias parameter is rejected at the $2\text{-}\sigma$ level. On the right side, we show the bias constraints using the 3PCF only. As can be seen from the results shown in Table ??, there is a slight disagreement in the best-fit values using only the 3PCF vs. using both the 2PCF and 3PCF.

5.2. LRG bias in real space

We explore here the validity of using redshift-space correlations to calculate galaxy bias parameters. When mapping the galaxies in the sky, we use the redshift of the galaxy as an indicator of distance. But since galaxies (and the dark matter) are subject to gravitational forces from the surrounding structures, peculiar velocities are added to the cosmological redshift, distorting our mapping of the large scale structure and as a consequence, the correlation functions are affected as well (see Hamilton 1998, for a review).

In the case of the 3PCF, there are differences between the real and redshift space 3PCF of galaxies and dark matter (eg. Gaztañaga & Scoccimarro 2005; Marín et al. 2008), and they will affect bias parameters as well. Marín et al. (2008), using mock galaxy catalogs, found good agreement, but not perfect, on the bias parameters in the L_* range, between using real or redshift space correlations, using $s \sim 10 h^{-1}\text{Mpc}$ configurations, and poorer agreement for brighter galaxies. That was caused by a combination of studying the bias using smaller scales (in the mildly non-linear regime) and by the small size of the box (only $200 h^{-1}\text{Mpc}$ on the side) for studying these galaxies which have a low spatial density.

As shown in Figure 8, on large scales (with $s \geq 15 h^{-1}\text{Mpc}$), for the mocks, the difference between the redshift and real space 3PCF is small and falls within the errors. In the case of the dark matter, there are differences, but because of the large bias, the mocks indicate that the LRG 3PCF will not show significant differences between the redshift and real space measurements on large scales.

In Figure 14 we show the differences in the correlation functions of dark matter and mock LRG galaxies from the N-body simulations by Sabiu et al. (2010), and how the bias parameters and σ_8 constraints change from using real and redshift space correlations. Note that on small scales there are significant differences between redshift and real space 3PCFs, but on larger scales, they are very similar. We have to keep in mind that these similarities occur this binning scheme, and might not be necessarily true with different 3PCF resolutions. For the 2PCF, the differences are small, but significant. For the bias constraints, note that real space measurements have a higher linear and non-linear bias, and usually the best-fit value of σ_8 is lower in the real space fits.

There have been analytical attempts to relate the real and redshift space 3-point function, in the case of the bispectrum (Scoccimarro et al. 1999; Smith et al. 2008), but there are practically no attempts of this in the configuration space, since non-linearities and mixing of large and small-scale modes makes the calculations very complicated unless one takes very simplified cases or do not

TABLE 2
 BEST-FIT BIAS PARAMETERS IN REDSHIFT SPACE

Sample	Triangles used	Fit	c_1	c_2	σ_8
DR7-Dim	$s \geq 10 h^{-1}\text{Mpc}$	2PCF & 3PCF, 3-parameter	$1.92^{+0.2}_{-0.1}$	$0.38^{+0.02}_{-0.08}$	$0.82^{+0.05}_{-0.13}$
DR7-Dim	$s \geq 15 h^{-1}\text{Mpc}$	2PCF & 3PCF, 3-parameter	$2.02^{+0.2}_{-0.1}$	$0.58^{+0.12}_{-0.08}$	$0.76^{+0.05}_{-0.07}$
DR7-Bright	$s \geq 10 h^{-1}\text{Mpc}$	2PCF & 3PCF, 3-parameter	$1.92^{+0.2}_{-0.1}$	$0.55^{+0.12}_{-0.15}$	$0.84^{+0.04}_{-0.05}$
DR7-Bright	$s \geq 15 h^{-1}\text{Mpc}$	2PCF & 3PCF, 3-parameter	$1.95^{+0.2}_{-0.1}$	$0.27^{+0.15}_{-0.08}$	$0.87^{+0.06}_{-0.07}$
DR7-Dim	$s \geq 15 h^{-1}\text{Mpc}$	2PCF & 3PCF, $\sigma_8 = 0.9$	$1.72^{+0.02}_{-0.02}$	$0.31^{+0.05}_{-0.05}$	-
DR7-Dim	$s \geq 15 h^{-1}\text{Mpc}$	2PCF & 3PCF, $\sigma_8 = 0.8$	$1.93^{+0.02}_{-0.02}$	$0.45^{+0.05}_{-0.05}$	-
DR7-Dim	$s \geq 15 h^{-1}\text{Mpc}$	3PCF 2-parameter	$1.83^{+0.12}_{-0.1}$	$0.32^{+0.12}_{-0.05}$	-
DR7-Bright	$s \geq 15 h^{-1}\text{Mpc}$	2PCF & 3PCF, $\sigma_8 = 0.9$	$1.95^{+0.02}_{-0.02}$	$0.32^{+0.1}_{-0.1}$	-
DR7-Bright	$s \geq 15 h^{-1}\text{Mpc}$	2PCF & 3PCF, $\sigma_8 = 0.8$	$2.18^{+0.02}_{-0.02}$	$0.51^{+0.1}_{-0.1}$	-
DR7-Bright	$s \geq 15 h^{-1}\text{Mpc}$	3PCF 2-parameter	$2.05^{+0.1}_{-0.1}$	$0.48^{+0.1}_{-0.1}$	-
DR7-Dim	-	Z08 HOD fit $\sigma_8=0.8$	2.22	0.55	-
DR7-Bright	-	Z08 HOD FoF fit $\sigma_8=0.8$	2.36	0.79	-

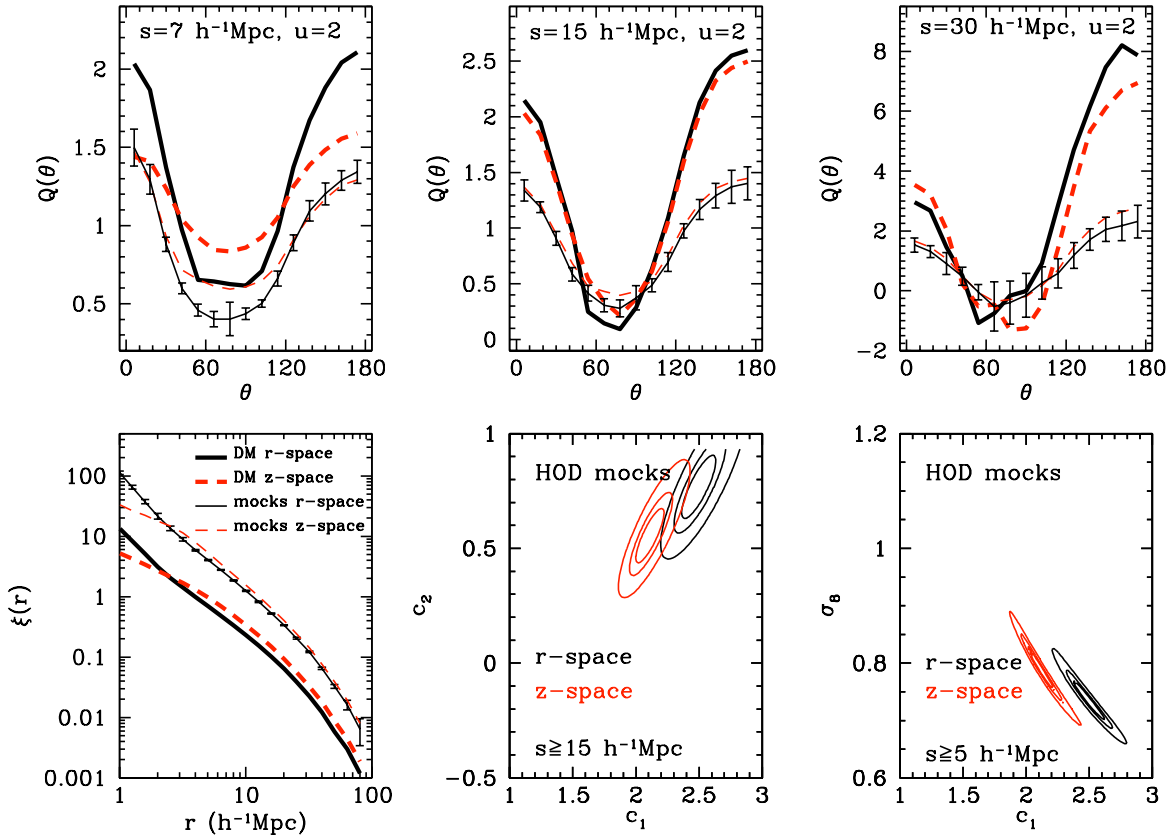


FIG. 14.— Redshift distortions in the 2PCF, 3PCF and in bias constraints. *Top panels*: 3PCF for different configurations, for dark matter in real (thick black solid line) and redshift space (thick red dashed line), and for HOD mocks in real (thin black line, with error bars) and redshift space (thin dashed line). *Bottom left*: 2PCF for dark matter and mocks in real and redshift space. *Bottom, middle and right*: Constraints in bias parameters c_1 and c_2 , and in σ_8 in real and redshift space. The contours are $\Delta\chi^2 = 1.0, 2.3$ and 6.2

take full advantage of the shape dependence of the 3-point statistics (eg., Pan & Szapudi 2005; Sefusatti et al. 2006) In our case, we take an empirical approach.

Using the similarity between the mock LRG 3PCF in real and redshift space for the large scales, we estimate constraints on the bias and σ_8 parameters using the real space dark matter correlations, and identifying the real space 3PCF with the redshift space 3PCF. In the case of the 2PCF, since the differences between real and redshift space correlations are significant, we will use the first-

order linear approximation in the case of redshift distortion (Kaiser 1987). Following Pan & Szapudi (2005):

$$\xi_{gal}^{z\text{-space}} = \left(1 + \frac{2}{3}f + \frac{1}{5}f^2\right) c_1^2 \left(\frac{\sigma_8}{0.8}\right)^2 \xi_{dm}^{r\text{-space}}, \quad (16)$$

where $f = \Omega_m^{0.6}/c_1$; we tested this prescription for our HOD mocks and it works well on the largest scales $r > 10 h^{-1}\text{Mpc}$. The results are shown in Figure 15, for both the LRG-Dim and LRG-Bright samples, using triangles with $s \geq 15 h^{-1}\text{Mpc}$. In general we see the same trend

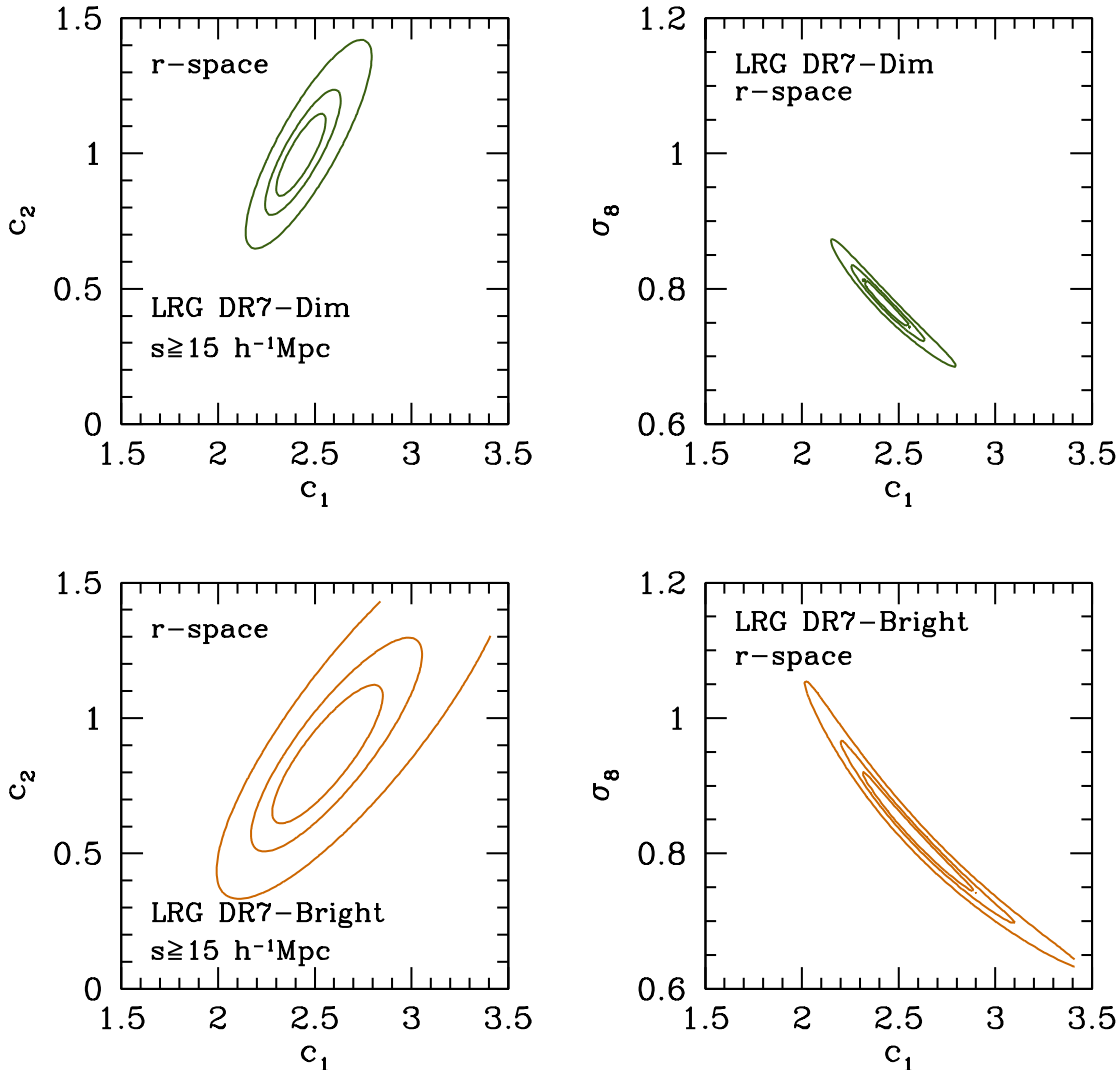


FIG. 15.— Marginalized bias parameters and σ_8 confidence intervals from joint 2PCF-3PCF fit for LRGs in real space for the DR7-Dim (top) DR7-Bright (bottom) LRG samples using the prescription described in §5.2. Only $s \geq 15 h^{-1}\text{Mpc}$ configurations are used. The contours are $\Delta\chi^2 = 1.0, 2.3,$ and 6.2 .

that was seen in Figure 14: both c_1 and c_2 are higher in real space, and we get reasonable constraints on σ_8 . We notice that here the constraints are in good agreement with the values obtained from the HOD fit of by Zheng et al. (2009) (shown in Table 3).

5.3. HOD constraints from large-scale bias

It is possible to use the bias parameters constraints to estimate best-fit values on the LRG HOD parameters. In Appendix A we show how it is possible to extract the large-scale bias parameters from the HOD, where only the average of the HOD function $\langle N(M) \rangle$ is needed to obtain the bias parameters b_1^h and b_2^h . Given the uncertainties in c_1, c_2 from the 3PCF, and for a fixed σ_8 , it is possible in principle to obtain constraints on HOD parameters (Sefusatti & Scoccimarro 2005) from large-scale bias parameters. We exemplify this using the LRG DR7-Dim sample.

There are many models for the mean $\langle N(M) \rangle$, with dif-

ferent number of parameters. It is worth mentioning that even though the meaning of common HOD parameters such as M_{min}, M_1 and α is similar for different functional forms of $\langle N(M) \rangle$, the best fit parameters can change significantly depending on the function used (Zheng et al. 2005). For the sake of simplicity, and to avoid marginalizing over many parameters, we use a simple model that uses three parameters, with a soft function for $N_{cen}(M)$ (Sefusatti et al. 2006; Kulkarni et al. 2007):

$$\langle N(M) \rangle = N_{cen}(M) + N_{sat}(M), \quad (17)$$

$$N_{cen} = \exp(-M_{min}/M), \quad (18)$$

$$N_{sat} = \exp(-M_{min}/M) \left(\frac{M}{M_1} \right)^\alpha. \quad (19)$$

We effectively constrain the HOD parameters M_1 and α , since we fix the spatial density of model galaxies to the mean density of the sample, and in practice, this constrains M_{min} .

TABLE 3
BEST-FIT BIAS PARAMETERS IN REAL SPACE

Sample	Triangles used	Fit	c_1	c_2	σ_8
DR7-Dim	$s \geq 10 h^{-1}\text{Mpc}$	2PCF & 3PCF, 3-parameter	$2.51^{+0.15}_{-0.1}$	$0.82^{+0.12}_{-0.04}$	$0.75^{+0.03}_{-0.02}$
DR7-Dim	$s \geq 15 h^{-1}\text{Mpc}$	2PCF & 3PCF, 3-parameter	$2.38^{+0.2}_{-0.1}$	$0.92^{+0.1}_{-0.1}$	$0.77^{+0.02}_{-0.05}$
DR7-Bright	$s \geq 10 h^{-1}\text{Mpc}$	2PCF & 3PCF, 3-parameter	$2.22^{+0.2}_{-0.1}$	$0.75^{+0.2}_{-0.1}$	$0.91^{+0.1}_{-0.1}$
DR7-Bright	$s \geq 15 h^{-1}\text{Mpc}$	2PCF & 3PCF, 3-parameter	$2.45^{+0.45}_{-0.25}$	$0.79^{+0.4}_{-0.1}$	$0.85^{+0.1}_{-0.1}$

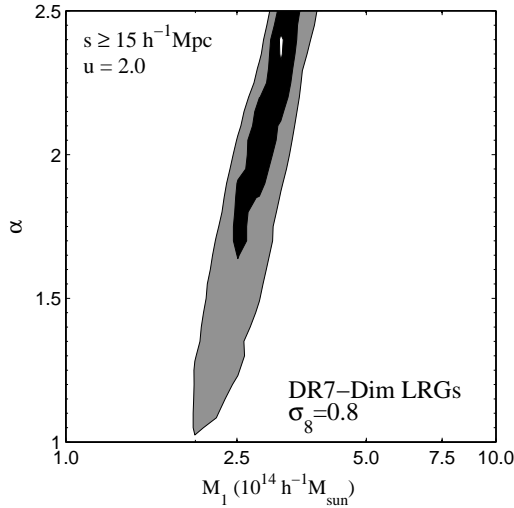


FIG. 16.— Constraints in HOD parameters M_1 and α from real-space bias measurements, when triangles with $u = 2$ and $s \geq 10 h^{-1}\text{Mpc}$ are used. The white point is the position of the best-fit HOD parameters. The contours are $\Delta\chi^2 = 2.3$, and 6.2, from inside out

We create a grid with different values of M_1 and α , where we calculate the bias parameters $b_1^h = c_1$ and $b_2^h = c_1 c_2$ (see Appendix A), and then we relate and use the results for the constraints on the bias parameters c_1 and c_2 of the DR7-Dim sample when we fix $\sigma_8 = 0.8$. This gives us a likelihood on the values of M_1 and α HOD parameters.

In Figure 16 we show the constraints on M_1 and α using the constraints on c_1 and c_2 for the DR7-Dim LRG sample, using $s \geq 15 h^{-1}\text{Mpc}$ configurations, for fixed $\sigma_8 = 0.8$. We notice the constraints are not very strong, especially on α . The best-fit HOD parameters, $M_1 = 3.2 \times 10^{14} h^{-1}\text{M}_\odot$, and $\alpha = 2.35$, and the constraints on M_1 are consistent with what is expected from fits to 2-point correlations, and although our best fit value for α is high, it is consistent with the findings of high α for the LRG HOD (Blake et al. 2008; Zheng et al. 2009), and higher from the estimates from 3PCF fits by Kulkarni et al. 2007. Note that the strongest constraints are on M_1 , and comparing the shape of these contours with the contours of Figure 13, we can conclude that M_1 , the “average” mass of a halo containing at least two LRGs (a central and a satellite) is mostly controlled by the linear bias c_1 , and α is more sensitive to the c_2 constraints.

6. CONCLUSIONS AND FUTURE DIRECTIONS

The purpose of this work was to show that the LRG 3PCF provides a complementary way to estimate biasing

and place constraints on cosmological models. With the advent of new and larger surveys, it is possible to get constraints comparable to other methods, in cosmology and galaxy population models. Our main findings are:

- With a new binning scheme, it is possible to have a better measurement of $Q(\theta)$ and go to larger scales, making it possible to use the LRG 3PCF to learn about galaxy bias and σ_8 .
- The measurement of error in the 3PCF is non-trivial. From measuring the 3PCF both in mocks and JK subsamples, we find that the covariance matrices have noticeable differences, and JKs tends to overestimate the errors and covariance compared to using mocks.
- Using the redshift space 2PCF and 3PCF, we estimate constraints on the linear and non-linear bias parameters. We show that the non-linear bias is non-zero at the 2σ level for LRGs.
- Using N-body simulations, for this binning scheme, we find that the predicted LRG 3PCF is very similar (within the errors) for real and redshift space measurements on large scales. Using this fact, we estimate bias parameters in real space, as well as σ_8 , which gives similar results to WMAP5 estimates.
- From the large-scale bias parameter constraints, we estimate HOD parameters. Our constraints are not very strong, but the best-fit values are similar to what is found by other methods.

Using a new binning scheme that preserves the shape dependence of $Q(\theta)$, it is possible to measure the 3PCF on a larger range of scales with a better signal-to-noise than previous schemes. We treated here the statistical errors only, but future investigations (outside the scope of this particular work) need also to address the issue of how different resolutions, or binning schemes, can lead to systematic errors in the 3PCF measurements and on bias constraints.

The measurement of errors shows that, provided that the mocks we use describe adequately the correlations of the sample which is analyzed, it is much preferable to use these instead of JK resampling as a method to calculate the covariance of 3PCF measurements. As opposed to the case of the 2PCF (eg Zehavi et al. 2005b), where the JK provide a good description, in the 3PCF we would need much larger volumes and even there, measure only on a limited range of scales, to be able to trust the JK error measurements. This is more of a problem when we

are talking about the covariance of the 3PCF measurements. For diagonal errors, it is possible to obtain them using a small number of subsamples $N \sim 10$, but to have a converged covariance matrix, $N \gtrsim 100$ are needed.

The aspects mentioned above will affect the model constraints from the 3PCF, and we will work on these aspects as well in future investigations. We showed that LRGs, or equivalently, high-mass galaxies have a high (non-zero) positive non-linear bias, and a confirmation from what is predicted by the halo and HOD models: that high mass galaxies (and halos) have large values of the linear and nonlinear bias parameters.

For larger scales, we take advantage of the fact that the LRG real space 3PCF is similar to the redshift space counterpart. With better measurements this might not be possible to do, especially if the purpose is to obtain more precise constraints on σ_8 , but the constraints obtained are consistent with what is expected from simulations, and moreover, they allow us to put complementary constraints on galaxy occupation models.

The future of the LRG 3PCF looks promising: apart from better constraints on biasing, on small scales HOD fits will become relevant, and on the largest scales, constraints from the BAO will also contribute to constraining cosmological and galaxy formation models.

The author thanks Joshua Frieman, for his encouragement in the research of high-order clustering in both theory and observations. Also many thanks to thank Cristiano Sabiu for facilitating his dark matter halo catalogs, to Jeremy Tinker for making available his HOD code, and to Daniel Eisenstein and Eyal Kazin for making their LRG data and random catalogs available, and to Roman Scoccimarro for making his dark matter halo catalogs available in the early steps of this research. The author is grateful to Robert Nichol and Risa Wechsler, for their initial and continuing inspiration to study the LRG 3PCF. Additional thanks to thank Hsiao-Wen Chen, Scott Doelsson, and Andrey Kravtsov, Enrique Gaztañaga, Emiliano Sefusatti, Idit Zehavi, Chris Blake and Cameron

McBride for useful suggestions and comments. This work was supported in part by the Kavli Institute for Cosmological Physics at the University of Chicago through grants NSF PHY-0114422 and NSF PHY-0551142 and an endowment from the Kavli Foundation and its founder Fred Kavli. Some of the calculations used in this work have been performed on the Joint Fermilab-KICP Supercomputing Cluster, supported by grants from Fermilab, Kavli Institute for Cosmological Physics, and the University of Chicago. The author thanks ICG Portsmouth and KIPAC/SLAC for their hospitality where initial stages of this work took place.

Funding for the SDSS and SDSS-II has been provided by the Alfred P. Sloan Foundation, the Participating Institutions, the National Science Foundation, the U.S. Department of Energy, the National Aeronautics and Space Administration, the Japanese Monbukagakusho, the Max Planck Society, and the Higher Education Funding Council for England. The SDSS Web Site is <http://www.sdss.org/>.

The SDSS is managed by the Astrophysical Research Consortium for the Participating Institutions. The Participating Institutions are the American Museum of Natural History, Astrophysical Institute Potsdam, University of Basel, University of Cambridge, Case Western Reserve University, University of Chicago, Drexel University, Fermilab, the Institute for Advanced Study, the Japan Participation Group, Johns Hopkins University, the Joint Institute for Nuclear Astrophysics, the Kavli Institute for Particle Astrophysics and Cosmology, the Korean Scientist Group, the Chinese Academy of Sciences (LAMOST), Los Alamos National Laboratory, the Max-Planck-Institute for Astronomy (MPIA), the Max-Planck-Institute for Astrophysics (MPA), New Mexico State University, Ohio State University, University of Pittsburgh, University of Portsmouth, Princeton University, the United States Naval Observatory, and the University of Washington.

This work is presented as a dissertation to the Department of Astronomy and Astrophysics, The University of Chicago, in partial fulfillment of the requirements for the Ph.D. degree.

REFERENCES

- Abazajian, K., Zheng, Z., Zehavi, I., Weinberg, D. H., Frieman, J. A., Berlind, A. A., Blanton, M. R., et al. 2005, *ApJ*, 625, 613
 Abazajian, K. N. et al. 2009, *ApJS*, 182, 543
 Berlind, A. A., & Weinberg, D. H. 2002, *ApJ*, 575, 587
 Bernardeau, F., Colombi, S., Gaztañaga, E., & Scoccimarro, R. 2002, *Phys. Rep.*, 367, 1
 Blake, C., Collister, A., & Lahav, O. 2008, *MNRAS*, 385, 1257
 Cooray, A., & Sheth, R. 2002, *Phys. Rep.*, 372, 1
 Davis, M., Efstathiou, G., Frenk, C. S., & White, S. D. M. 1985, *ApJ*, 292, 371
 Eisenstein, D. J. et al. 2001, *AJ*, 122, 2267
 —. 2005, *ApJ*, 633, 560
 Frieman, J. A., & Gaztanaga, E. 1994, *ApJ*, 425, 392
 Fry, J. N., & Gaztanaga, E. 1993, *ApJ*, 413, 447
 Gaztañaga, E., Cabré, A., Castander, F., Crocce, M., & Fosalba, P. 2009a, *MNRAS*, 399, 801
 Gaztañaga, E., Cabré, A., & Hui, L. 2009b, *MNRAS*, 399, 1663
 Gaztañaga, E., Norberg, P., Baugh, C. M., & Croton, D. J. 2005, *MNRAS*, 364, 620
 Gaztañaga, E., & Scoccimarro, R. 2005, *MNRAS*, 361, 824
 Gray, A. G., Moore, A. W., Nichol, R. C., Connolly, A. J., Genovese, C., & Wasserman, L. 2004, in *ASP Conf. Ser.* 314: *Astronomical Data Analysis Software and Systems (ADASS) XIII*, 249
 Guzik, J., & Seljak, U. 2002, *MNRAS*, 335, 311
 Hamilton, A. J. S. 1998, in *Astrophysics and Space Science Library*, Vol. 231, *The Evolving Universe*, ed. D. Hamilton, 185+
 Jing, Y. P., & Börner, G. 2004, *ApJ*, 607, 140
 Jing, Y. P., Mo, H. J., & Boerner, G. 1998, *ApJ*, 494, 1
 Kaiser, N. 1987, *MNRAS*, 227, 1
 Kayo, I. et al. 2004, *PASJ*, 56, 415
 Kazin, E. A. et al. 2010, *ApJ*, 710, 1444
 Komatsu, E. et al. 2009, *ApJS*, 180, 330
 Kravtsov, A. V., Berlind, A. A., Wechsler, R. H., Klypin, A. A., Gottlöber, S., Allgood, B., & Primack, J. R. 2004, *ApJ*, 609, 35
 Kulkarni, G. V., Nichol, R. C., Sheth, R. K., Seo, H.-J., Eisenstein, D. J., & Gray, A. 2007, *MNRAS*, 378, 1196
 Landy, S. D., & Szalay, A. S. 1993, *ApJ*, 412, 64
 Marín, F. A., Wechsler, R. H., Frieman, J. A., & Nichol, R. C. 2008, *ApJ*, 672, 849
 Masjedi, M. et al. 2006, *ApJ*, 644, 54

- McBride, C. K., Connolly, A. J., Gardner, J. P., Scranton, R., Newman, J. A., Scoccimarro, R., Zehavi, I., & Schneider, D. P. 2010, ArXiv e-prints
- McBride et al. 2010b, in preparation
- Moore, A. W. et al. 2001, in *Mining the Sky*, 71
- Navarro, J. F., Frenk, C. S., & White, S. D. M. 1997, *ApJ*, 490, 493
- Nichol, R. C. et al. 2006, *MNRAS*, 368, 1507
- Pan, J., & Szapudi, I. 2005, *MNRAS*, 362, 1363
- Peebles, P. J. E. 1980, *The Large-Scale Structure of the Universe* (Princeton University Press)
- Peebles, P. J. E., & Groth, E. J. 1975, *ApJ*, 196, 1
- Percival, W. J. et al. 2007, *ApJ*, 657, 645
- Press, W. H., & Schechter, P. 1974, *ApJ*, 187, 425
- Reid, B. A., & Spergel, D. N. 2009, *ApJ*, 698, 143
- Ross, A. J., & Brunner, R. J. 2009, *MNRAS*, 399, 878
- Ross, A. J., Brunner, R. J., & Myers, A. D. 2008, *ApJ*, 682, 737
- Sabiú et al. 2010, in preparation
- Scoccimarro, R., Couchman, H. M. P., & Frieman, J. A. 1999, *ApJ*, 517, 531
- Scoccimarro, R., Sheth, R. K., Hui, L., & Jain, B. 2001, *ApJ*, 546, 20
- Sefusatti, E., Crocce, M., Pueblas, S., & Scoccimarro, R. 2006, *Phys. Rev. D*, 74, 023522
- Sefusatti, E., & Scoccimarro, R. 2005, *Phys. Rev. D*, 71, 063001
- Seljak, U. 2000, *MNRAS*, 318, 203
- Sheth, R. K., Mo, H. J., & Tormen, G. 2001, *MNRAS*, 323, 1
- Sheth, R. K., & Tormen, G. 2002, *MNRAS*, 329, 61
- Smith, R. E., Sheth, R. K., & Scoccimarro, R. 2008, *Phys. Rev. D*, 78, 023523
- Szapudi, I. 2005, arXiv:astro-ph/0505391
- Szapudi, S., & Szalay, A. S. 1998, *ApJ*, 494, L41
- Tegmark, M. et al. 2006, *Phys. Rev. D*, 74, 123507
- Tinker, J., Kravtsov, A. V., Klypin, A., Abazajian, K., Warren, M., Yepes, G., Gottlöber, S., & Holz, D. E. 2008, *ApJ*, 688, 709
- White, S. D. M., & Rees, M. J. 1978, *MNRAS*, 183, 341
- York, D. G., et al. 2000, *AJ*, 120, 1579
- Zehavi, I. et al. 2005a, *ApJ*, 621, 22
- , 2004, *ApJ*, 608, 16
- Zehavi, I., et al. 2005b, *ApJ*, 630, 1
- Zheng, Z. et al. 2005, *ApJ*, 633, 791
- Zheng, Z., & Weinberg, D. H. 2007, *ApJ*, 659, 1
- Zheng, Z., Zehavi, I., Eisenstein, D. J., Weinberg, D. H., & Jing, Y. P. 2009, *ApJ*, 707, 554

APPENDIX

A. LRG HOD AND LARGE-SCALE BIAS

A.1. Halo Mass Function

The distribution of dark matter halos is biased with respect to the dark matter (Press & Schechter 1974), therefore the galaxies, formed inside these halos, are biased tracer as well. As mentioned above, in the HOD model we proceed in two steps: First, we described how dark matter halos are distributed in the universe, and second, how galaxies populate these halos.

To describe the mass function of dark matter halos (i.e., the spatial density of halos as a function of mass) we use the Sheth & Tormen mass function (Sheth et al. 2001; Sheth & Tormen 2002):

$$n_h(M) = \frac{\bar{\rho}_m}{M^2} \left| \frac{d \ln \sigma}{d \ln M} \right| f(\nu) \quad (\text{A1})$$

where $\bar{\rho}_m \equiv \Omega_M \rho_c$ is the average matter density in the universe at the epoch of observation, $\nu = \delta_c / \sigma(M, z)$, with $\delta_c = 1.69$ the threshold for growth of linear fluctuations, and σ , the r.m.s. variance of a sphere of radius $R(M)$ at redshift z :

$$\sigma^2(R, z) = \int \frac{d^3 k}{(2\pi)^3} |W(k, R)|^2 P(k, z). \quad (\text{A2})$$

Here $P(k, z)$ is the linear matter power spectrum and $W(k, R)$ is the Fourier transform of a top-hat window of radius R . The function $f(\nu)$ is motivated by the ellipsoidal collapse model (Sheth & Tormen 2002) and has the form

$$f(\nu) = A \sqrt{\frac{2a\nu^2}{\pi}} [1 + (a\nu^2)^{-p}] e^{-a\nu^2/2}, \quad (\text{A3})$$

where for normalization $A = 0.322$, $p = 0.3$ and $a = 0.707$.

A.2. HOD bias

Knowing the probability function $P(N|M)$ of how galaxies populate halos as a function of mass, we can infer the clustering at any scale. The HOD model allow us, knowing the mean occupation number $\langle N(M) \rangle$, in the large-scale limit to estimate the bias parameters:

$$b_i = \frac{1}{n_g} \int_{M_{min}}^{\infty} dM n_h(M) b_i^h(M) \langle N_g(M) \rangle, \quad (\text{A4})$$

where $i=1,2$ represent the linear and first non-linear bias term, $n_h(M)$ the dark matter halo mass function, $b_i^h(M)$ is the halo bias and $\langle N_g(M) \rangle$ is the mean number of galaxies for a halo of mass M , and n_g is the galaxy number density, calculated as:

$$n_g = \int_{M_{min}}^{\infty} dM n_h(M) \langle N(M) \rangle, \quad (\text{A5})$$

The dark matter halo bias parameters are given by Scoccimarro et al. (2001)

$$b_1^h(M) = 1 + \epsilon_1 + E_1 \quad (\text{A6})$$

$$b_2^h(M) = \frac{8}{21} (\epsilon_1 + E_1) + \epsilon_2 + E_2 \quad (\text{A7})$$

the coefficients given by

$$\epsilon_1 = \frac{a\nu^2 - 1}{\delta_c}, \quad (\text{A8})$$

$$\epsilon_2 = \frac{a\nu^2(a\nu^2 - 3)}{\delta_c^2}, \quad (\text{A9})$$

$$E_1 = \frac{2p}{\delta_c(1 + (a\nu^2)^p)}, \quad (\text{A10})$$

$$\frac{E_2}{E_1} = \frac{1 + 2p}{\delta_c} + 2\epsilon_1. \quad (\text{A11})$$

It is worth emphasizing that the bias relations mentioned in equation (A4) are only valid on large scales, in the quasi-linear regime, and they are scale independent. On smaller scales the bias becomes very scale-dependent and higher moments of the $P(N|M)$ function need to be known.